THE JOURNAL OF COMPARATIVE NEUROLOGY 425:560–582 (2000)

Fundamental GABAergic Amacrine Cell Circuitries in the Retina: Nested Feedback, Concatenated Inhibition, and Axosomatic Synapses

ROBERT E. MARC[1]* AND W.-L.S. LIU[2]
[1]John Moran Eye Center, University of Utah School of Medicine, Salt Lake City, Utah 84132
[2]Houston, Texas

ABSTRACT

Presynaptic γ-aminobutyrate-immunoreactive (GABA+) profiles were mapped in the cyprinid retina with overlay microscopy: a fusion of electron and optical imaging affording high-contrast ultrastructural and immunocytochemical visualization. GABA+ synapses, deriving primarily from amacrine cells (ACs), compose 92% of conventional synapses and 98% of the input to bipolar cells (BCs) in the inner plexiform layer. GABA+ AC synapses, the sign-inverting elements of signal processing, are deployed in micronetworks and distinctive synaptic source/target topologies. Nested feedback micronetworks are formed by three types of links (BC → AC, reciprocal BC ← AC, and AC → AC synapses) arranged as nested BC↔ [AC → AC] loops. Circuits using nested feedback can possess better temporal performance than those using simple reciprocal feedback loops. Concatenated GABA+ micronetworks of AC → AC and AC → AC → AC chains are common and must be key elements for lateral spatial, temporal, and spectral signal processing. Concatenated inhibitions may represent exceptionally stable, low-gain, sign-conserving devices for receptive field construction. Some chain elements are GABA immunonegative (GABA−) and are, thus, likely glycinergic synapses. GABA+ synaptic baskets target the somas of certain GABA+ and GABA− cells, resembling cortical axosomatic synapses. Finally, all myelinated intraretinal profiles are GABA+, suggesting that some efferent systems are sources of GABAergic inhibition in the cyprinid retina and may comprise all axosomatic synapses. These micronetworks are likely the fundamental elements for receptive field shaping in the inner plexiform layer, although few receptive field models incorporate them as functional components. Conversely, simple feedback and feedforward synapses may often be chimeras: the result of an incomplete view of synaptic topology. J. Comp. Neurol. 425:560–582, 2000.

Indexing terms: immunocytochemistry; digital imaging; electron microscopy

Most vertebrate retinal neurons use γ-aminobutyric acid (GABA) or glutamate as a primary fast neurotransmitter (Massey, 1990; Marc et al., 1990; Marc, 1992; Kalloniatis et al., 1996; Kalloniatis and Tomisch, 1999; Thoreson and Witkovsky, 1999). In cyprinid fishes, independent arrays of ≈15 types of bipolar cells (BCs) cells form synaptic complexes with subsets of ≈70 types of amacrine cells (ACs), the majority of which are likely to be GABAergic (Scholes, 1975; Wülle and Wagner, 1990; Marc, 1992; Sherry and Yazulla, 1993). Subsets of BCs are themselves sampled by at least 15 ganglion cell (GC) types (Hitchcock and Easter, 1986), leading to the view that a cyprinid retina generates ≈15 filtered versions of the visual world. The shaping of GC receptive fields in all vertebrate retinas appears to be dominated by GABAergic AC feedback and feedforward (Marc, 1992), although the weights and true forms of these paths are unknown. As an example, most of the AC input to type Mb ON-center BC axon terminals in

Grant sponsor: NIH; Grant number: EY02576; Grant sponsor: Research to Prevent Blindness Jules and Doris Stein Research to Prevent Blindness Professorship.

*Correspondence to: Robert E. Marc, Moran Eye Center, University of Utah, 75 North Medical Dr., Salt Lake City, UT 84132.
E-mail: robert.marc@hsc.utah.edu

Received 4 April 2000; Revised 12 June 2000; Accepted 14 June 2000

the goldfish retina is associated with GABAergic markers (Marc et al., 1978; Yazulla et al., 1987; Marc, 1989; Muller and Marc, 1990), and these structural data are supported by physiologic demonstrations of GABA-activated hyperpolarizations and Cl^- conductance increases, as well as inhibition of a voltage dependent Ca^{+2} current in Mb BCs (Kondo and Toyoda, 1983; Tachibana and Kaneko, 1987; Matthews et al., 1994). Yet after all this time and effort, the functional circuitries underlying even the simplest of GC receptive fields remain unknown and only fragmentary views of the essential micronetworks from which they are assembled exist. The goals of our investigations were to quantitatively map GABAergic connectivity in the inner plexiform layer and explore the conventional connective patterns (feedback, feedforward, serial synapses) that we expected were essential to descriptions of receptive field organization. In the end, we concluded that inhibitory circuitry is far richer than simple feedforward and feedback; that other synaptic micronetworks and arrangements are common and important in retinal signal processing. Indeed, a simple feedback or feedforward circuit may not even exist in the cyprinid inner plexiform layer and might be, at best, a fragmentary view of the true micronetworks underlying receptive field properties.

This richer inhibitory circuitry is partly reflected in synaptic arrangements designated as *nested feedback* and *nested feedforward*. The formal circuit topologies of simple inverting feedback and feedforward (e.g., Marmarelis and Marmarelis, 1978) are illustrated in Figure 1A, with BC → AC and BC → GC paths as afferent sign-conserving stages and BC ← AC and AC → GC paths as sign-inverting feedback and feedforward, respectively. Simple feedback can be symbolized as BC ↔ AC and is realized anatomically as the classic reciprocal feedback synapse of BC dyads (e.g., Dowling, 1968). Nested structures arise from topologic loops within larger elements. Nested feedback/feedforward is simple feedback/feedforward augmented by a loop wherein the inverting AC targets itself (Fig. 1B). The structure is formally nested in the sense that the AC → AC loop is internal to the BC ↔ AC feedback loop. This is anatomically realized as pairs of AC processes driven by one BC, with one AC targeting the other (Fig. 1C). If both AC processes are part of the same AC or separate cells of the same type, the topology of Figure 1C is formally equivalent to Figure 1B. Even if both AC processes are different cell types, the local micronetwork is equivalent to Figure 1B. Nested feedback can be symbolized as BC ↔ [AC → AC]. Much of the synaptology we will describe suggests that nested feedback and feedforward are common structures in the inner plexiform layer.

Electron microscopic autoradiographic analyses enabled discovery of basic forms of GABAergic circuitry in the vertebrate inner plexiform layer (Marc et al., 1978; Nakamura et al., 1980; Pourcho, 1981; Yazulla, 1981; Freed et al., 1983: Pourcho and Goebel, 1983; Muller and Marc, 1990; for reviews see Marc, 1992 and Freed, 1992). However, deducing connective rules from these analyses has always been compromised by poor spatial resolution and limited sample sizes. Direct visualization of GABA content by hapten-conjugate immunocytochemistry (Storm-Mathisen et al., 1983) is now a preferred marker for the study of retinal circuitry (e.g., Studholme and Yazulla, 1988; Koontz et al., 1993), providing the highest available spatial resolution for retinal synaptic mapping. Even so, descriptions of synaptic patterns have been compromised by limited sampling and, more seriously, the inability to account for sampling errors in immunocytochemical preparations (see Appendix). Both electron microscopic autoradiography and immunogold immunocytochemistry yield high and often unspecified high false-negative rates, i.e., instances where true GABA+ synapses are incorrectly scored as GABA−. With these concerns in mind, we used registration methods taken from remote sensing imaging to align light microscopic GABA signals with serial electron microscopic images and view them as transparent overlays, hence the term, *overlay microscopy*. The method provides optimal ultrastructural visualization, near-optimal signal to noise properties, and very low false-negative rates.

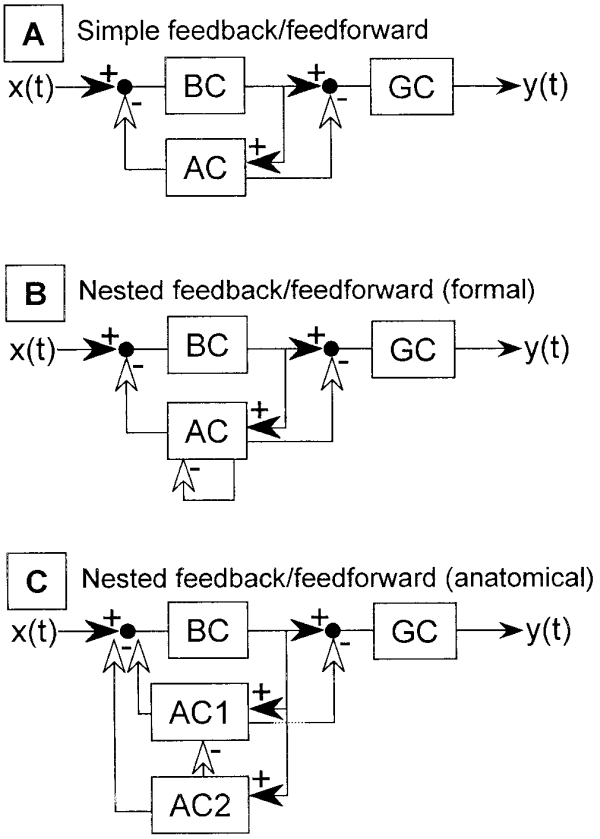

Fig. 1. Forms of inverting feedback/feedforward. **A:** Simple feedback and feedforward among a bipolar cell (BC), amacrine cell (AC), and ganglion cell (GC), where x(t) is the formal time-varying input and y(t) is the time-varying output. Sign-conserving signal transfers are coded as black arrows and marked +; sign-inverting signal transfers are coded as white arrows and marked −. **B:** Formal nested feedback/feedforward adds a single inverting loop to the AC segment of the circuit. **C:** In biologic systems, nested feedback/feedforward might be visualized as involving two distinct AC profiles labeled AC1 and AC2, both driven by a single BC.

MATERIALS AND METHODS

Tissue harvest

Goldfishes were killed by cervical transection and double pithing and retinas isolated and fixed for electron

microscopy as previously described (e.g., Marc et al., 1988b). All animal care and experimental protocols conformed to the Institutional Animal Care and Use Committee guidelines of the University of Utah.

Electron microscopy

Conventional transmission electron microscopy was performed at 80 Kv on 90 nm lead stained sections of aldehyde fixed, osmicated goldfish retina. Sections were carbon coated and supported on Formvar film (Pelco) on single hole grids. Most of the data reported are derived from a vertical section (S371) encompassing a 745 μm length of central retina prepared for light microscopic analysis of GABA immunoreactivity and matched to a serial section prepared for electron microscopy. The entire inner plexiform layer was photographed at a magnification of 6,170×, referenced to a carbon lattice. The collection was printed at a final magnification of 19,127×, montaged onto ten 8 foot × 4 foot rigid panels and covered with 5-mil acetate. Additional data regarding patterns of BC innervations were obtained from a 42-section series of the inner plexiform layer and other samples of GABA immunoreactivity.

Ultrastructural analysis

Structures of interest from S371 were marked on a 30 × 40 cell grid of scaled 1-μm squares superimposed on the acetate cover each panel, and the positions of 5,397 structures were coded into a database. The apparent geometric center was visually estimated for structures larger than 1 μm^2. Not all the recorded structures are reported in this study. The ones of interest herein include BC terminals of Ma, Mb, branching and varicose cone BC types; all BC synaptic ribbons; BC → AC synapses; BC → presumed GC synapses; AC → BC synapses; AC → AC synapses; reciprocal feedback synapses; myelinated profiles; and profiles containing dense-cored vesicles. Histograms of laminar distributions were constructed with 20 bins of 1.5 μm average bin width.

Conventional synapses, ribbon synapses and myelinated processes were identified by widely accepted criteria, but special consideration was given to BC profiles lacking ribbons. Omission of uranyl acetate en bloc staining preserves a range of cytoplasmic gray levels allowing unambiguous identifications of BC terminals in cyprinids (e.g., Witkovsky and Stell, 1973; Marc et al., 1988a). BCs in such material are more electron-opaque than other neural profiles, contain a large population of vesicles that uniformly fill the terminals (Witkovsky and Dowling, 1969), and possess a unique crenelated profiles indented by surrounding elements. Goldfish retinal GC axons are myelinated within the optic fiber layer, but other myelinated processes enter and course through the inner plexiform layer in fishes. These have been interpreted as efferent (centrifugal) fibers (Witkovsky and Dowling, 1969; Witkovsky, 1971). Only myelinated profiles within the distal and proximal limits of the inner plexiform layer were coded.

Light microscopy and immunocytochemistry

A single 90-nm gold section consecutive to each electron microscopic section was collected onto a glass spot slide (HTC slide, Cel-Line, Inc.), deplasticized in sodium methoxide, deosmicated with sodium periodate, and processed for postembedding immunocytochemistry with anti-GABA IgGs and silver intensification immunogold visualization as previously detailed (Marc et al., 1990; 1995). For the quantitative analyses of connectivity, the entire inner plexiform layer of S371 and samples of the inner plexiform layers of other preparations were photographed with a Zeiss 100× planapochromatic objective onto Kodak TMAX 100 film and stored as individual negatives in anti-Newton frames. Additional material sectioned in both vertical and horizontal planes was probed with anti-GABA, anti-glycine, and anti-glutamate IgGs (Signature Immunologics, Inc., Salt Lake City, UT) and visualized as described in Marc et al. (1995).

Digital database formation

Digital databases were created by scanning transilluminated negatives at 300–2,400 dpi as needed on a Microtek Scanmaker 5 (Microtek International, Inc., Taiwan). Electron microscopic mosaics of the inner plexiform layer were formed from 6–20 tiles and stored as 4,096 × 4,096 (4K × 4K) low-resolution images. Electron microscopic negative images were inverted, high-pass sharpened, and contrast-adjusted if needed in PhotoShop® 5.0 (Adobe Systems, Mountain View, CA). Such operations altered neither the raw data nor assignments of profiles. Light microscopic negatives were contrast adjusted, set the maximum and minimum pixel values to 255 and 0, respectively, but not inverted. After registration (see below), the scaled, aligned light and electron microscopic frames were combined in a single image (Marc et al., 1995) with GABA+ regions coded as an image layer. The GABA+ regions were colorized, the edges darkened for visibility and the colored layer superimposed on the electron microscopic layer with multiplicative transparency in PhotoShop® 5.0.

Mosaicking and registration

Electron microscopic tiles were mosaicked with subpixel precision (PCI Remote Sensing, Arlington, VA) as previously described (Marc et al., 1995). Briefly, scaling, rotation, translation, and shear in image space were determined by selecting 20–50 control points (identical locations in overlapping image pairs) and calculating values for pixel relocation with 1st or higher order models. Higher order models were useful in correcting subtle aberrations such as section distortion or magnification astigmatism near the edges of electron microscopic (EM) negatives. The final master image of 6–20 tiles could then be similarly registered with the light microscopic data and subregions of the image selected for high-resolution visualization.

Accurate registration requires identification of unambiguous control points such as somatic/nuclear margins, Müller's cell stalks, and myelinated fibers. Because the sections were serial and, thus, not identical, many control points spread across the image were required for good local fits. It is physically impossible to "hand-register" scaled photographs of such data as absolute scaling, correction of astigmatisms, and shear corrections can only be extracted mathematically. Mismatches between electron and light microscopic images caused by mechanical distortion or electron-optical aberrations were assayed by registering a standardized grid with the transformation model derived from control points for a pair of images. The maximal distortion encountered was a 9% displacement linear stretch.

Performance measures for overlay microscopy

The capacity of overlay microscopy to resolve small profiles as GABA+ or GABA− is partly constrained by the Rayleigh limit. A reasonable resolution limit might be expected to be approximately 250 nm, which is smaller than most of the synaptic terminals we sought to characterize. However, some postsynaptic profiles are small dendrites less than 250 nm in diameter and, as the serial sections are displaced 90 nm, direct assessments of resolution performance are critical. The resolution of a system is also impacted by the probability of making an error based on signal strength. Thus, we sought to compare performance factors of overlay microscopy with those of other visualization methods such as immunocytochemistry and autoradiography. For simplicity, these comparisons are presented in the Appendix. In general, overlay microscopy proved to have better signal-detection properties than any other electron microscope imaging method. It also exhibited good spatial resolution, surpassing that of electron microscope autoradiography, equivalent to most electron microscope immunogold methods, and inferior only to the best immunogold and enzyme-linked implementations.

Image preparation

All images were imported into Adobe PhotoShop 5.0 ® as gray-scale TIFF files. All optical and electron microscope images were contrast-adjusted by using the linear MAX-MIN method, which is equivalent to selecting paper contrast and exposure time in photographic printing. Color RGB mapping was executed as previously published (Marc et al., 1995) by inverting each gray-scale signal and assigning each image to a color channel. Colored overlay microscopy images were produced by converting the optical GABA signal channel to a PhotoShop® PSD file format layer, removing all zero value background pixels by cutting, colorizing the remaining pixels with hue value 40, saturation 100, and lightness −20. This converts pure white pixels into a light orange tint with RGB coordinates 255, 219, 153. The electron microscopic channel is then displayed through a transparent layer in the multiplicative mode, generating a highly saturated colored signal representing GABA immunoreactivity. In some low-magnification images, the edges of the GABA signal were enhanced by outlining the tinted region with a three pixel border of darker color.

Nested feedback modeling

The possible effects of nested feedback were explored with the modular modeling tool Extend 3.2.1 (Imagine That, Inc., San Jose, CA). BCs and excitatory inputs were modeled as filtered amplifiers yielding sign-conserving responses to an impulse input with gains of two and alpha-like response shapes. Inhibitory inputs were modeled as filtered amplifiers yielding sign-inverting responses with gains of 0.75 and alpha-like response shapes. Power spectra were visualized as response FFTs with no windowing and 128 data points. Model responses were exported to Microsoft Excel® and thence to Microsoft PowerPoint® for generating illustrations. The model file is available upon request.

RESULTS

Processes of GABA+ ACs dominate every level of the goldfish inner plexiform layer

Processes of GABA+ ACs fill the inner plexiform layer (Fig. 2A), finely sculpting the GABA− profiles of Müller cells, BCs, glycinergic ACs, GCs, etc. so precisely that one can easily envision combining optical and ultrastructural data. The reliability of the GABA signal can be illustrated by viewing a horizontal section through the AC layer as a gray-scale GABA image (Fig. 2B) and comparing it with a version that displays concurrent GABA, glycine, and glutamate signals as an RGB mapping. In particular, glutamate-rich BCs and all glycine+ ACs can been seen as completely invisible to the anti-GABA IgG.

The details of the AC populations and process patternings in the inner plexiform may be further quantified by classifying GABA, glycine, glutamate, taurine, and glutamine signals in the inner plexiform layer (Marc et al., 1995), thus extracting the fractional composition of each signal type. From these and similar data, it is possible to account for the inner plexiform layer as ≈80% GABA+ AC signals, 2% glycine+ AC signals, 2% GC signals, 6% BC signals, and 10% Müller's cells. The residual volume of dopaminergic interplexiform cell signals is far less than 0.5% of the inner plexiform layer. These values correspond well to absolute counts we will document in this manuscript. If effectively all conventional synapses in the inner plexiform layer arise from GABA+ and glycine+ profiles and the number of synapses per unit dendritic volume is constant for all cell types, then ≈96% of all AC profiles should be GABA+, ignoring a small reduction for dopaminergic junctions and an unknown increment for efferents. We determined that 92% of the 1,763 conventional synapses counted in this report were GABA+ and that the small difference is likely due to a nonlinear relation between dendritic volume and synapse number for GABA+ and glycine+ ACs.

We will not attempt a comprehensive description of goldfish AC types in this report, beyond noting that the AC layer itself contains a heterogeneous set of somas representing a mixture of ACs, BCs, Müller cells (Fig. 2), and occasional displaced GCs (Marc et al., 1990). Although early estimates of glycinergic ACs suggested that they represented upward of one-third of all ACs, more recent analyses revealed that 50–75% of glycine+ elements in the AC layer have the metabolic phenotype of mammalian glycine-coupled BCs (Kalloniatis et al., 1996) and size of cone BC somas (Fig. 1C; see also Marc et al., 1995). Taking this into account, GABA+ ACs represent ≈85% and glycine ACs ≈15% of all ACs. This better matches direct measurements of synaptic frequencies, but still suggests that glycine+ ACs make fewer synapses per cell than GABA+ ACs. Correlative studies with other cellular marking methods have previously shown that ACs can be partitioned into generic morphologic types such as pyriform, radiate, multipolar bistratified, and even starburst/coronate morphologies (e.g., Ammermüller and Weiler, 1981; Wagner and Wagner, 1988; Marc et al., 1993) and most of these must be GABA+.

Forms of GABAergic connectivity

In previous work, we demonstrated that optical sections as thin as 40 nm can be precisely registered to reveal concurrent amino acid contents across all cell types and

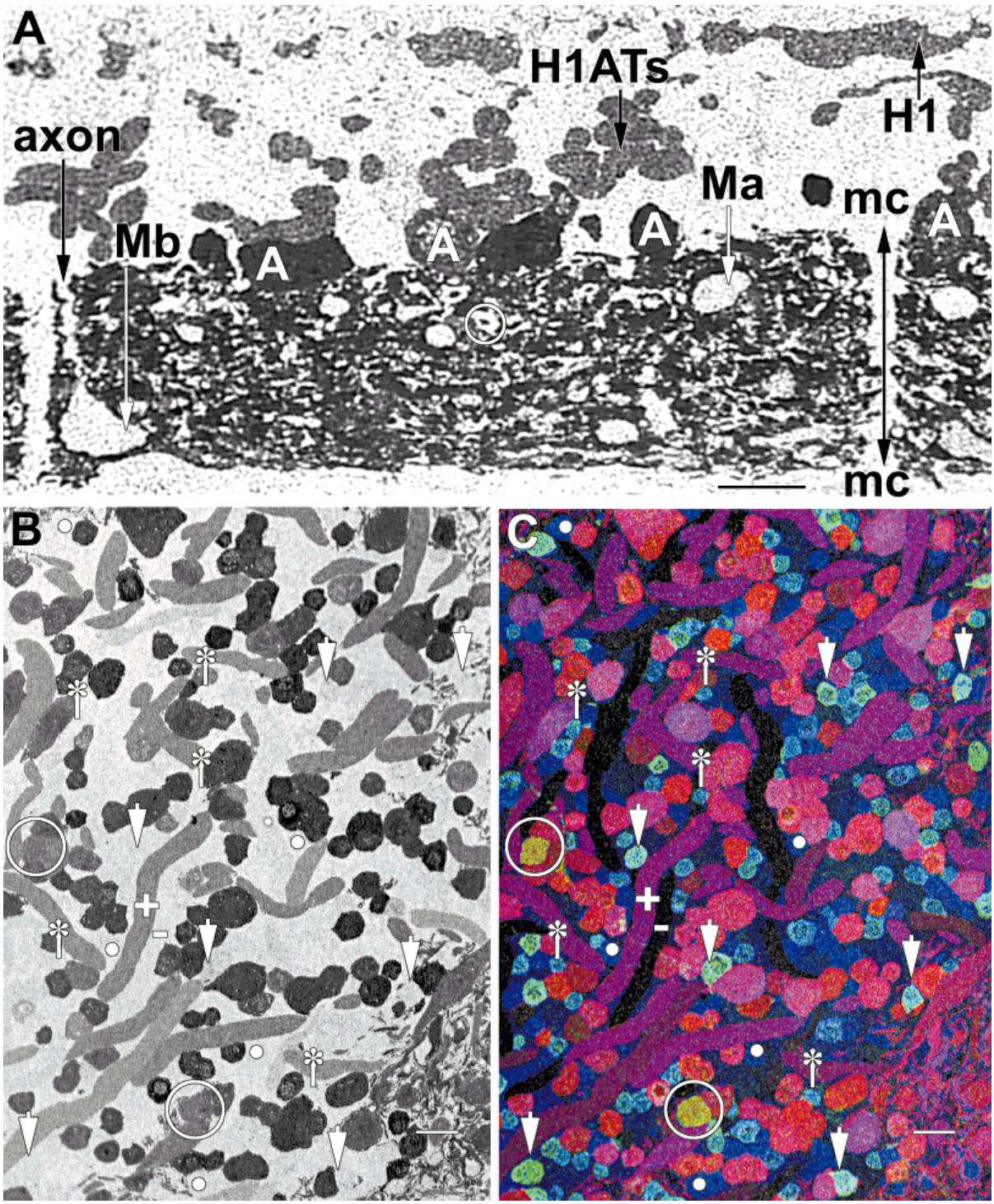

Fig. 2. γ-Aminobutyrate (GABA) -ergic amacrine cells (ACs) and patterning in the goldfish retina. **A:** GABA signals in a 250-nm section, demonstrating the high signal-to-noise properties of optical microscopy. The section spans the retina from the outer plexiform layer (top) to the ganglion cell layer (bottom). H1 HCs and their axon terminals (H1ATs) characteristically display lower GABA content than most ACs (A). Key GABA-immunonegative elements in the inner plexiform layer are the proximal stalks of Müller cells (mc) and various bipolar cell (BC) terminals of which the mixed rod-cone OFF-center (Ma) and ON-center (Mb) types are the most distinctive. In well-oriented material, the axons of bipolar cells are also easily recognized. **B:** A horizontal 250-nm section through the AC layer, demonstrating the apparently absolute signal selectivity of the anti-GABA immunoglobulin G. Gray and black circular and polygonal structures indicate AC somas, and tuberous gray profiles represent H1 HC axon terminals (+). GABA-immunonegative HC axon terminals (−) are also abundant. The GABA-immunonegative space is composed of Müller cells (not marked), glycine+ ACs (arrowheads), glycine + cone BCs (asters), and many small BCs (dots). Two members of the sparse GI˙1 AC population are encircled. **C:** GABA, glycine, glutamate → *rgb* mapping of the AC layer. Serial 250-nm sections were consecutively probed for GABA, glycine, and glutamate signals and registered, revealing the characteristic spectral signatures of the elements marked in B. Scale bars = 10 μm in A–C.

structures. One can easily conceive, then, of inserting a single electron microscope image into such a series with equivalent precision. Registration of light and electron microscopic images revealed fine sculpting of BC terminals throughout the inner plexiform layer, demonstrating that both type Mb ON-center BCs (Fig. 3) and Mb OFF-center BCs (Fig. 4) are surrounded by a large number of GABA+ profiles. Although the alignment of the light and electron microscopic images cannot be perfect (they are serial and not identical images), the precision is nevertheless good. Misalignments are most common when a small process runs parallel to the plane of section. However, by simply examining the sizes and shapes of neighboring profiles to see whether they are possible signal sources, such errors are easily recognized. Even very small processes, such as those opposite the synaptic ribbon in Figure 4B, are readily classified as GABA+ or GABA−. Reciprocal feedback synapses between BCs and GABA+ ACs and *apparently* isolated conventional GABA+ AC synapses onto BCs are abundant in both types of BCs. In fact, all types of BC profiles in the inner plexiform layer were almost entirely surrounded by and are both presynaptic and postsynaptic to GABA+ AC terminals (e.g., Fig. 5A,B). On occasion, rare GABA− ACs were presynaptic to BC terminals (Fig. 4B). Assuming such profiles to be glycinergic is consistent with previous observations of a low density of glycinergic inputs to cyprinid BCs (Marc and Lam, 1981; Studholme and Yazulla, 1988; Muller and Marc, 1990). Vesicle-free GABA− neural profiles are rather infrequent, electron lucent with little cytoskeleton, and are presumed characteristic of the terminal dendritic processes of retinal GCs.

Myelinated fibers are common in cyprinid retinas (Witkovsky, 1971) and all of the profiles encased in myelin wraps were strongly GABA+ in our material (e.g., Fig. 5A). Because these retinas were isolated and preincubated in teleost saline before fixation, the glial wrapping around the axons had become loosened. Although this method does not faithfully represent the normal ultrastructure, it had the advantage of making such profiles particularly evident even at the optical level (Fig. 1A), because neither the glial membranes, the minimal glial cytoplasm, nor the extracellular space possessed any GABA immunoreactivity, rendering the GABA+ axons nicely delimited by a GABA− annulus. The axons themselves were neurofilament-rich at every level of the inner plexiform layer and contained but few microtubules (Fig. 5C). Myelinated processes are commonly located in the most distal and proximal strata of the inner plexiform layer, and all of them were GABA+. Large displaced GCs in the goldfish retina are all strongly glutamate immunoreactive and GABA immunonegative (Marc et al., 1990), indicating that these GABA+ profiles cannot be their descending axons. The GABA+ displaced ACs of the goldfish retina do not have identifiable axons when viewed by Golgi impreg-

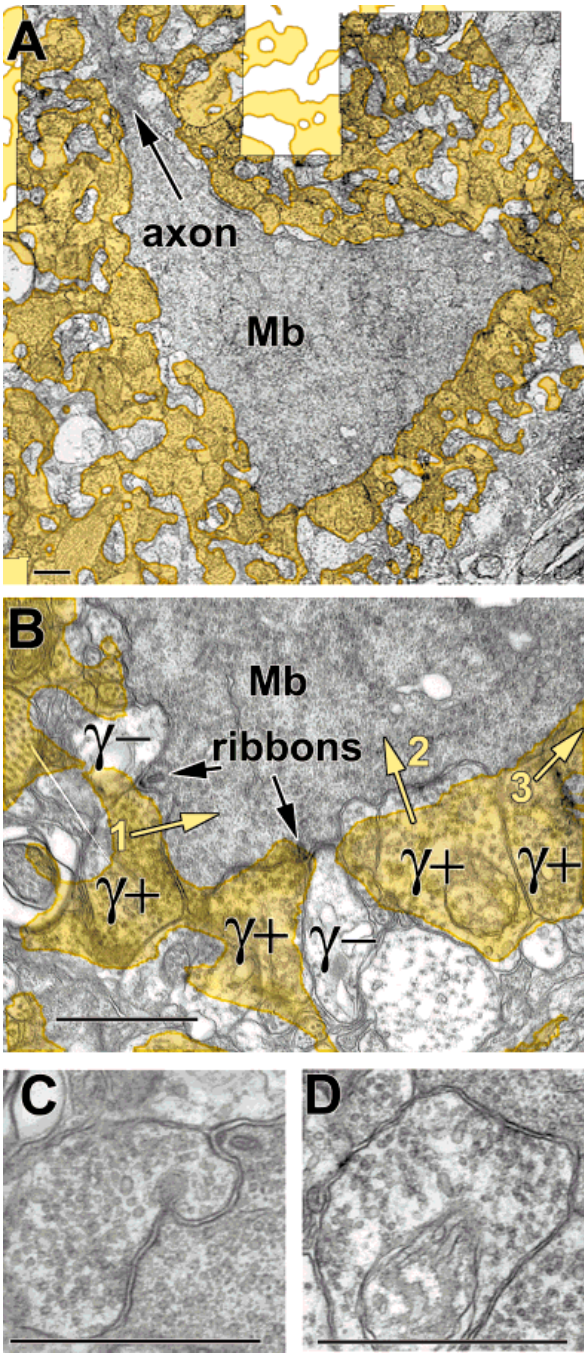

Fig. 3. γ-Aminobutyrate (GABA) immunoreactivity surrounding type Mb bipolar cell (BC) axon terminals visualized with overlay microscopy. All GABA-immunoreactive elements are visualized as a colored overlay from a registered serial 90 nm section captured by optical microscopy. **A:** A low-resolution mosaic of electron microscopic images, revealing the tight sculpting of the BC terminal by GABA+ profiles. The distal-proximal axis of the inner plexiform layer runs from the upper left to lower right. **B:** A higher resolution registration of the lower left corner of the BC terminal reveals GABA+ (γ+) amacrine cell (AC) profiles presynaptic (profiles 1,2; colored arrows) and postsynaptic (1) to the BC. Profile 3 targets an adjacent GABA+ element. GABA− (γ−) profiles have the characteristic vesicle- and cytoskeleton-poor features of terminal ganglion cell dendrites. **C:** A serial section of profile 1 in B. **D:** A serial section of profile 2 in B. Scale bars = 1 μm in A–D.

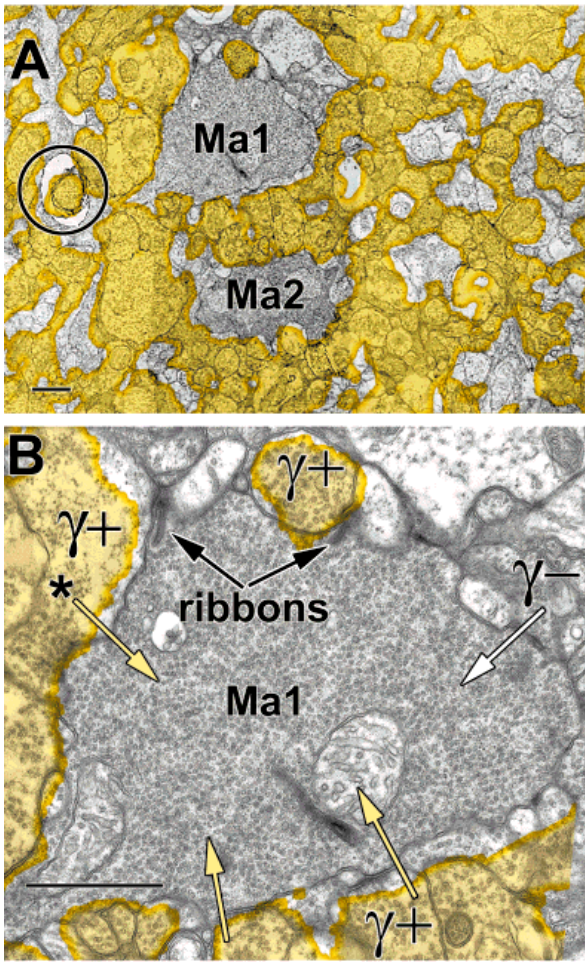

Fig. 4. γ-Aminobutyrate (GABA) immunoreactivity surrounding type Ma bipolar cell (BC) axon terminals visualized with overlay microscopy. **A:** A low-resolution mosaic of electron microscopic images, revealing the tight sculpting of the BC terminal by GABA+ profiles. Ma1 and Ma2 terminals are distinguished by their positions in the inner plexiform layer. A GABA+ myelinated process is circled. **B:** A higher resolution registration of the Ma1 terminal, demonstrating numerous GABA+ (γ+) presynaptic profiles (colored arrows), one of which is both presynaptic and postsynaptic to the BC (asterisk). A GABA− (γ−) profile is also presynaptic (white arrow). Scale bars = 1 μm in A,B.

nation or ChAT immunocytochemistry (Marc et al., 1993) and, in any case, intraretinal axons from ACs seem unlikely to be myelinated. Witkovsky (1971) demonstrated that some myelinated fibers in goldfish were (1) unequivocally of extraretinal origin, (2) identifiable by silver stains known to be preferential for neurofilament-rich processes, and (3) presynaptic to both BC terminals and AC somas. Our data suggest that the myelinated intraretinal fibers are a homogeneous population and perhaps represent a single type of fast inhibitory efferent pathway.

Several different arrangements of GABA+ connectivity were documented. In the dataset derived from sample S371, four GABA+ ACs and one GABA− AC (Fig. 6) were identified with GABA+ AC conventional synapses containing small, clear synaptic vesicles directly targeting the soma. One cell (Fig. 6A) displayed 6 GABA+ conventional synaptic inputs, suggesting that the soma was encased in a glomerulus of ≈100 synapses, assuming a single section to be representative of the density of inputs over the proximal surface of the cell. Because the S371 database included some 50 GABA+ AC somas and represented but a single section through an array of over 70 types of ACs (Wagner and Wagner, 1988), the discovery of 4 somas receiving GABA+ input suggests that this configuration is common, but selective for key cell types.

Alternatively, the primary targets of ACs in the inner plexiform layer are GCs and other ACs. Our particular concerns were the patterns of serial synapses involving GABA+ and GABA− ACs. GABA+ → GABA+ synapses and concatenations of three GABA+ profiles were remarkably common, especially considering the low probability of encountering AC synapses in series (Fig. 7). Profiles deemed likely to be GC dendrites based on their similarities to vesicle-free profiles seen opposite synaptic ribbons of BCs are as frequent a target as GABA+ AC dendrites. Clear cases of GABA+ → to GABA− AC synapses were less frequent as the overall density of GABA− systems is low, but are nonetheless distinctive (Fig. 8), including massive GABA+ input to GABA− ACs and GABA− AC input to GABA+ profiles. As will be revisited below, feedforward concatenation is abundant and a common mechanism in receptive field construction.

Distribution of GABAergic connectivity

The total distribution of conventional synapses in the inner plexiform layer is broadly bimodal with GABA+ profiles accounting for most of them (Fig. 9). The synapse density envelope roughly conforms to the probability of encountering GABA+ profiles, with the exception of the distal one-fifth of the inner plexiform layer, consistent with the fact that most profiles there must be "dendrites of passage" destined for more proximal targets in the inner plexiform layer. We presume that these synapses are nearly all attributable to ACs, except for those arising from efferents, which may comprise a significant fraction of synapses at the distal border of the inner plexiform layer. Figure 9A also shows the parsing of contacts onto differing targets, that is, 25% of all targets are BCs, 32% are GABA− and GABA+ AC and 42% are GCs. Because identifying GC profiles is difficult in goldfish tissue due to the great similarity of GC and AC processes in vesicle-free zones, this is a conservative estimate because only 8% of all unequivocal AC processes are GABA− by ultrastructural measures (4% by pattern recognition measures). Taking the larger number as the upper limit and assuming that we erroneously classified true GABA− ACs as GCs half the time, our assignment of targets would actually be 36% as ACs and 38% as GCs. No matter how we evaluate the data, it is clear that a massive flow of putative GABAergic signals converge on GCs.

Because only a tiny fraction of AC synapses are GABA−, their distribution is most easily viewed as the residuals from the mean level across the inner plexiform layer (Fig. 9B). GABA− synapses are rarer at the borders of the inner plexiform layer and richer in mid-inner plexiform layer, consistent with the distribution of glycine uptake systems (Marc, 1986) and glycine immunoreactivity in the goldfish (Studholme and Yazulla, 1988; Marc et

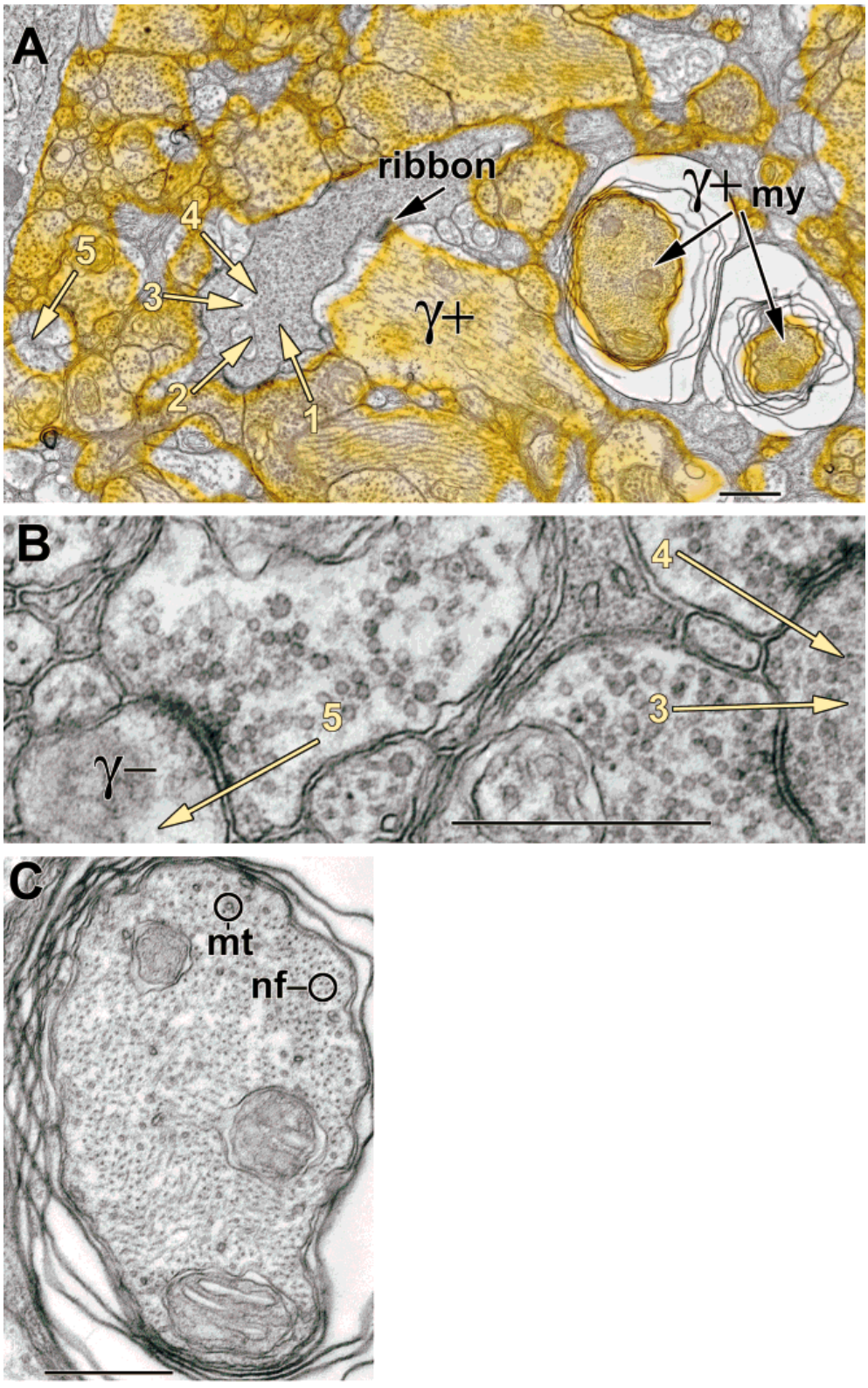

Fig. 5. γ-Aminobutyrate (GABA) immunoreactivity of myelinated profiles (my) and profiles surrounding unidentified bipolar cell (BC) axon terminals visualized with overlay microscopy. **A:** A small BC process at level 20 of the inner plexiform layer targets a large GABA+ process and receives input from four GABA+ profiles (colored arrows 1–4). A fifth GABA+ profile targets a nondescript element (colored arrow 5). **B:** Higher resolution views of GABA+ profiles 3,4,5. **C:** Higher resolution view of one myelinated profile in A, demonstrating characteristic sparse microtubule (mt) and high neurofilament content (nf). Scale bars = 500 nm in A,B; 250 nm in C.

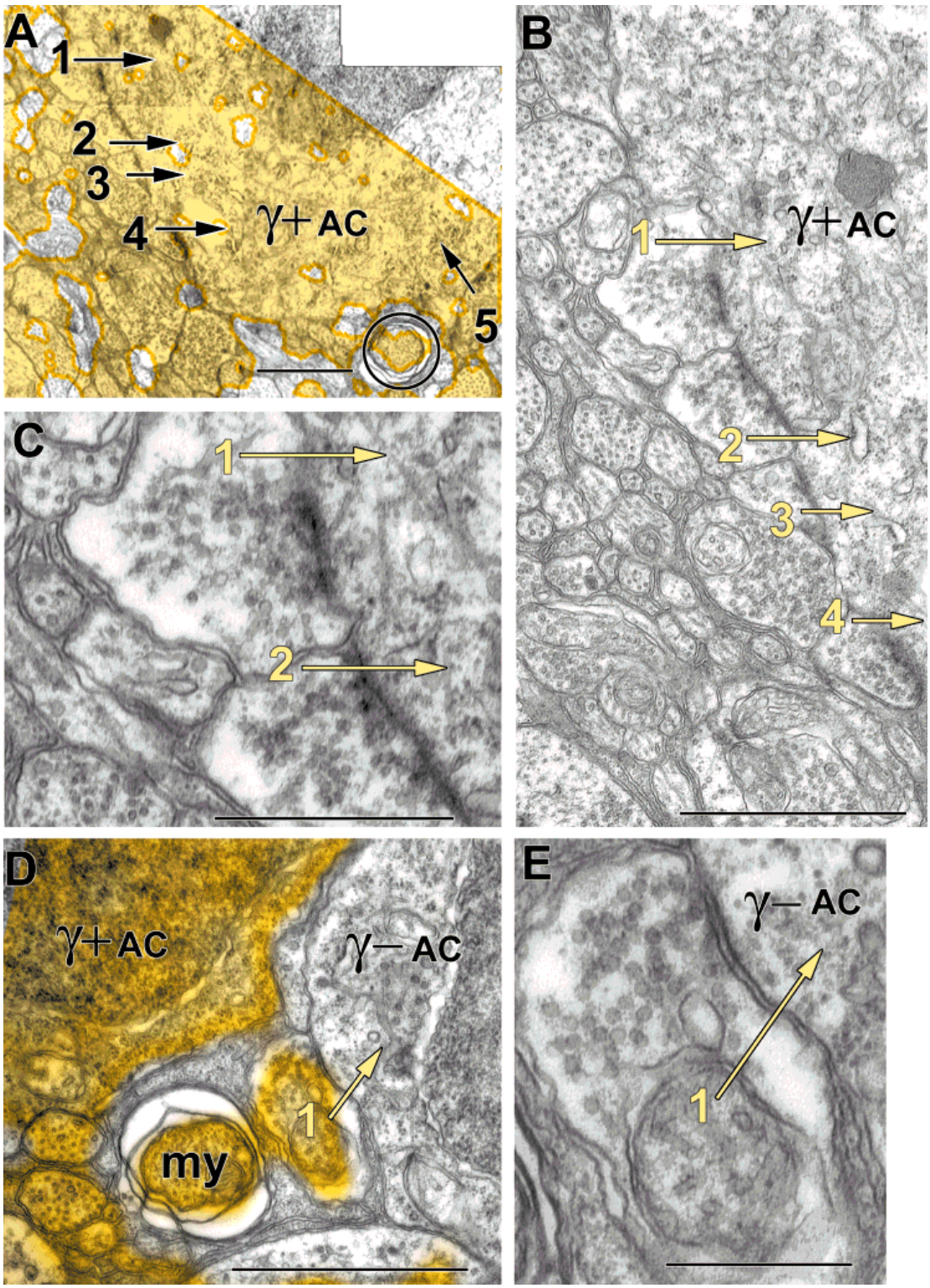

Fig. 6. γ-Aminobutyrate-immunoreactive (GABA+) synaptic input to GABA+ and GABA− amacrine cell (AC) somas visualized with overlay microscopy. **A:** A low-resolution mosaic of electron microscopic images demonstrating five GABA+ synapses (colored arrows 1–5) onto the soma of a GABA+ AC (γ + AC). A GABA+ myelinated profile is encircled. **B:** A medium resolution image of the GABA+ AC soma in A, revealing the high density of small, clear synaptic vesicles in the calyx of GABA+ profiles. **C:** Higher resolution image of profiles 1 and 2 in A showing the distinct, albeit obliquely cut postsynaptic densities of the AC soma. **D:** A low-resolution image of a GABA+ synapse into a GABA− AC (γ − AC)soma and a GABA+ myelinated (my) profile. **E:** Higher resolution image of the synapse made by GABA+ profile 1 in D. Scale bars = 1,000 nm in A,B,D; 500 nm in C,E.

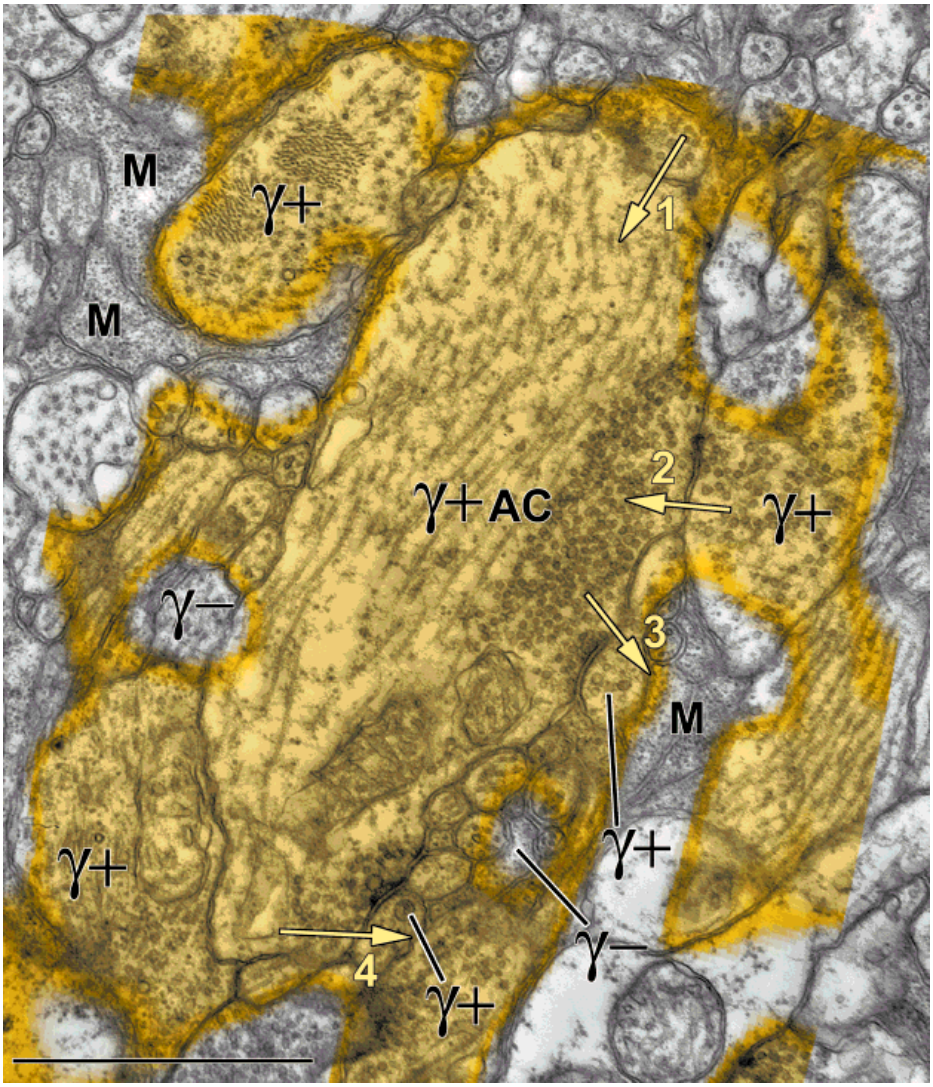

Fig. 7. Concatenated γ-aminobutyrate-immunoreactive (GABA+) synapses visualized with overlay microscopy. A single large GABA+ profile amacrine cell (γ+ AC) receives input from GABA+ (γ+) profiles at synapses 1 and 2 and targets two more GABA+ profiles at synapses 3 and 4. The GABA+ profiles are distinct from adjacent Müller cell elements (M) and small GABA− (γ−) neuronal profiles. Scale bar = 1,000 nm.

al., 1995). Thus, over 98% of all AC contacts at the proximal border of the inner plexiform layer are GABA+, whereas approximately 87% are GABA+ at level 50.

The BC innervation by ACs shows a rather strong bimodal pattern partly attributable to the frequency of BC terminals themselves (Fig. 9C). The incidence of synapses onto BCs in mid-inner plexiform layer is higher than expected from the frequency of BC terminals but, less obvious but likely more relevant, the number of GABA+ contacts onto distal BCs is actually less dense than expected if all BCs possessed the same relative proportions of GABA+ AC, GABA− AC, and GC contacts. Our impression is that many more GC contacts are made by type Ma BC terminals, thus reducing the number of GABA+ elements surrounding them relative to more proximal terminals (Fig. 9D). Although a quarter of all GABA+ AC synapses are targeted to BCs, actually only approximately 20% contact BCs in the range of levels 0–70. The most proximal region of the goldfish inner plexiform layer is characterized by type Mb BCs whose large terminals extend nearly to the GC layer and that command a large fraction of all AC input. Overall, 98% of all AC synapses on BCs are GABA+.

Myelinated processes are found in the proximal and distal thirds of the inner plexiform layer (Fig. 9E), tracking the distributions attributable to retinal efferents. Because some the efferent systems of some ectotherms have been shown to contain gonadotropins and/or FMRFamide-

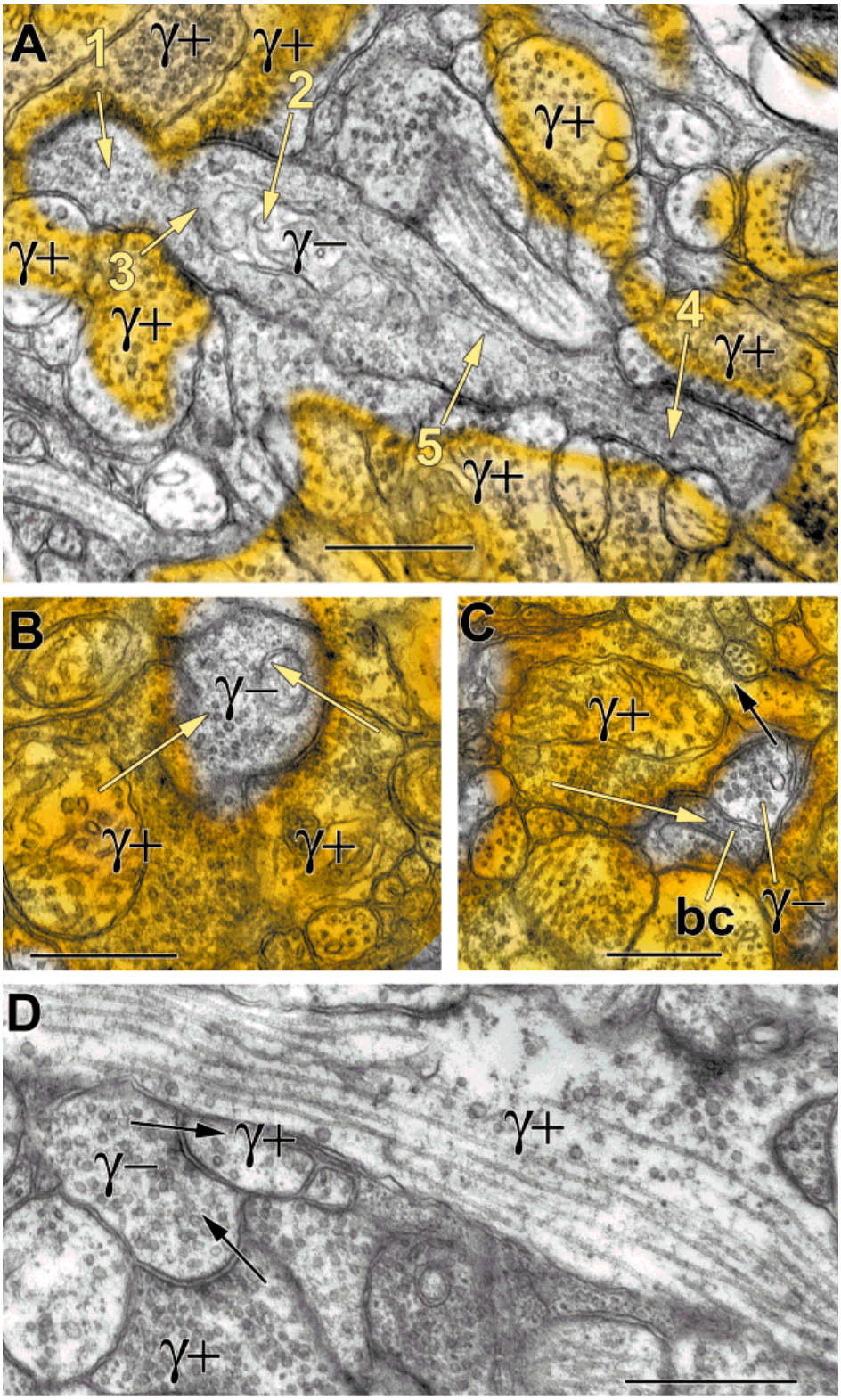

Fig. 8. Concatenated synaptic chains involving both γ-aminobutyrate-immunoreactive (GABA+) (γ+) and GABA− (γ−) profiles viewed by overlay microscopy. **A:** A large GABA− profile with the characteristic dark cytoplasm of glycinergic amacrine cells (ACs) receiving synaptic input from 5 GABA+ profiles. **B:** A small GABA− AC profile clasped between two GABA+ presynaptic profiles. **C:** A small GABA− AC profile presynaptic to a GABA+ profile that, in turn, targets a small element with the characteristic cytology of a bipolar cell (bc). **D:** A chain of GABA+ to GABA− to GABA+ AC profiles. Overlay color removed for clarity. Scale bars = 500 nm in A–D.

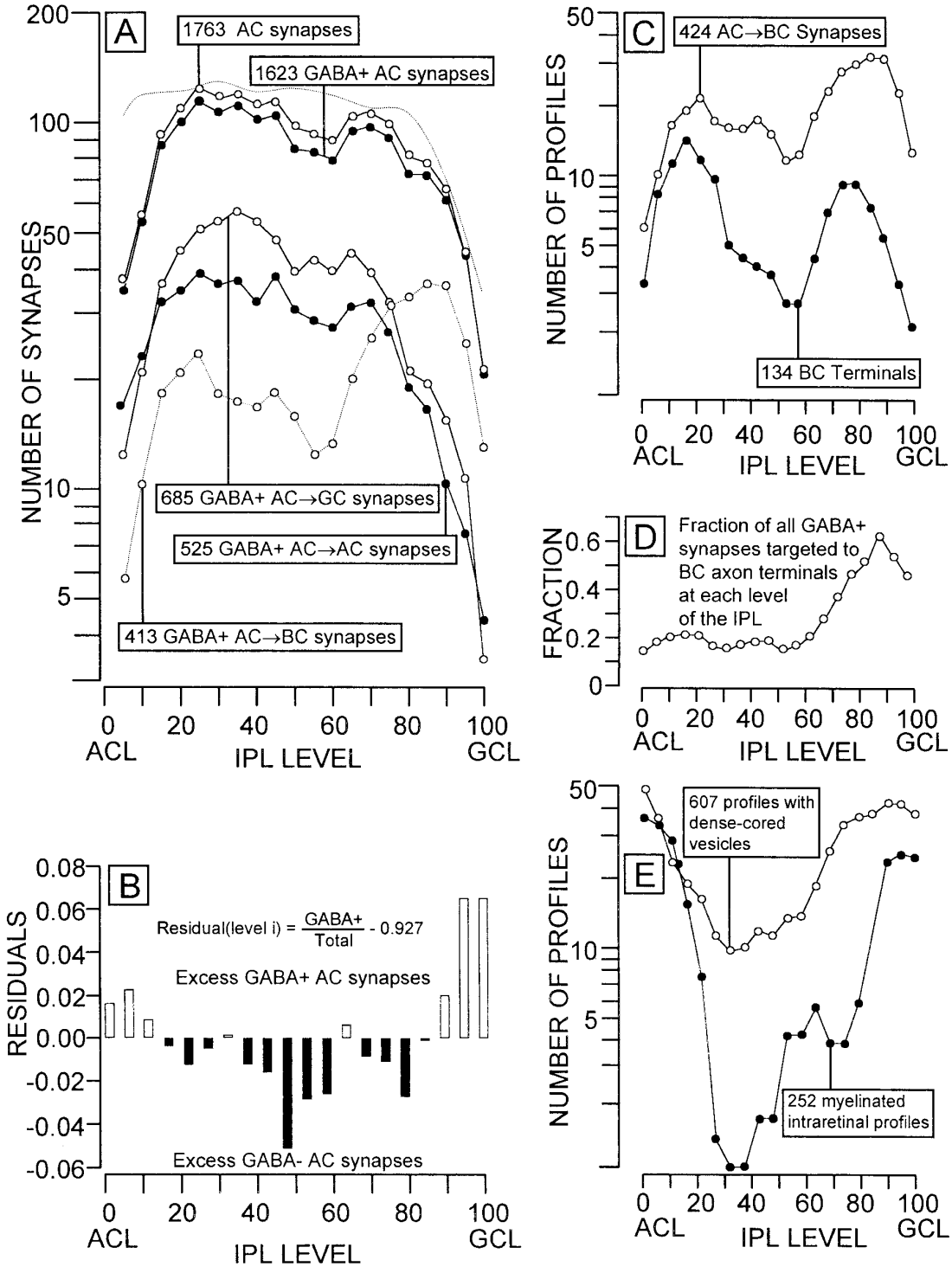

Fig. 9. Collected statistics of amacrine cell (AC) connectivity in the goldfish inner plexiform layer. **A:** The numbers of identified synapses encountered in the entire inner plexiform layer of sample S371 are plotted on a logarithmic ordinate at each level of the inner plexiform layer in 20 steps. The top dotted curve is the γ-aminobutyrate-immunoreactive (GABA+) profile probability curve from Figure 2. The successive underlying curves represent the total AC, the GABA+ AC, the GABA+ AC → ganglion cell (GC), the GABA+ AC → AC, and the GABA+ AC → bipolar cell (BC) synapse encounters with the curve totals indicated. **B:** The residual synapse frequency (the difference between the GABA+ fraction at each level and the total GABA+ mean) amplifies the small gap between total and GABA+ AC synapses shown in A. At the distal and proximal margins of the inner plexiform layer, GABA+ terminals dominate, whereas excess GABA− (presumably glycinergic) synaptic terminals are restricted to the middle two-thirds of the inner plexiform layer. **C:** Total AC → BC synapse distributions compared with the total BC terminal profile. **D:** The fraction of GABA+ synapses that target BC axon terminals across the inner plexiform layer. **E:** The distributions of myelinated profiles and profiles containing dense-cored vesicles across the inner plexiform layer.

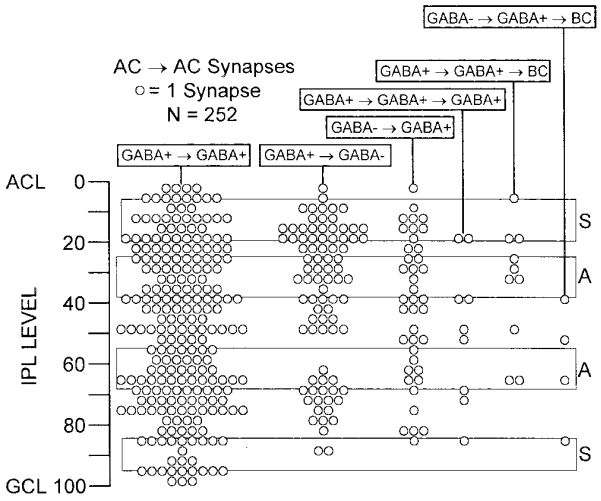

Fig. 10. The distribution of concatenated amacrine cell (AC) → AC synapses at all inner plexiform layer levels. Each circle represents a single synapse in which the γ-aminobutyrate-immunoreactive (GABA+) or GABA− signals of all elements in a synaptic chain were distinct. The zones of arborization of GABA+/serotoninergic (S) and GABA+/cholinergic (A) ACs are indicated by boxes. GCL, ganglion cell layer; ACL, amacrine cell layer; BC, bipolar cell; IPL, inner plexiform layer.

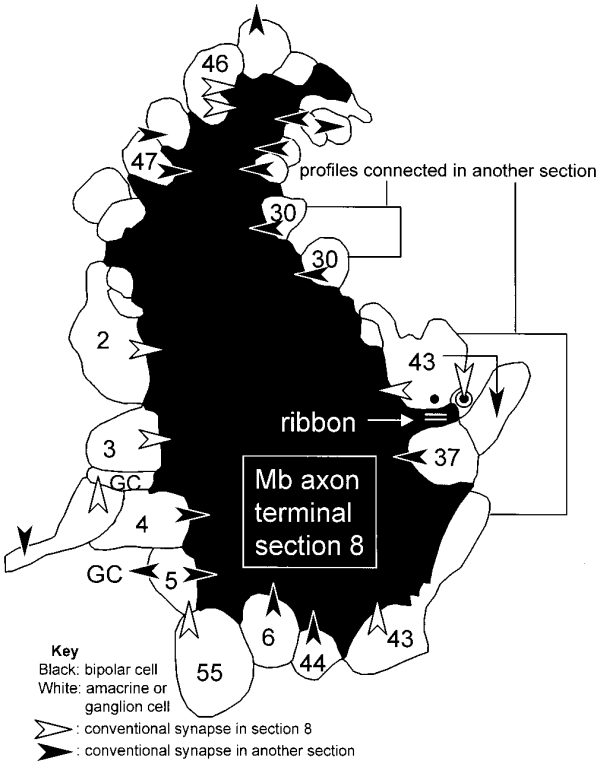

Fig. 11. A single schematic profile from a type Mb bipolar cell axon terminal (number 8 in a series of 42), indicating specific contacts with amacrine cells in that section (white arrows) and from the numbered profile in other serial sections.

like peptides (Stell et al., 1984, 1987; Zucker and Dowling, 1987; Uchiyama et al., 1988), we also mapped all profiles containing at least two dense-cored vesicles and obtained a distribution roughly similar to the one described by Marshak et al. (1988). Although the distributions of dense-cored vesicles and myelinated profiles are roughly similar, we have no direct evidence that the GABA+ myelinated profiles contain a peptide signal and dense-cored vesicles were sparse in the myelinated profiles. The profile of myelinated elements is provocative, as it drops to nearly zero in the middle of the inner plexiform layer. We interpret this finding to mean that there are really quite few myelinated efferents arising from the optic nerve, but that they branch heavily in the distal and proximal inner plexiform layer, consistent with images of Golgi-impregnated efferents in avian retinas (Ramón y Cajal, 1892; Cowan and Powell, 1963). In fact, the incidence of GABA+ myelinated profiles is so high at level 10 of the inner plexiform layer (Fig. 9E) that they might account for nearly all conventional synapses therein (Fig. 9A).

The chains of AC synapses involving GABA+ elements are distributed throughout the inner plexiform layer, but even with a sample of over 1,700 contacts, chains of three are rarer simply because their much lower encounter probability. Figure 10 summarizes the locations of 252 well-defined concatenations in the database of S371. The GABA+ > GABA+ doublet occurs throughout the inner plexiform layer. Some of these signals involve GABAergic-serotoninergic ACs (Marc et al., 1988b; Ball and Tutton, 1990) and GABAergic-cholinergic ACs (Marc et al., 1993). However, neither cell group accounts for all of the GABA+ signals at a given level of the inner plexiform layer and GABAergic-serotoninergic cells in particular account for only 5% of GABA+ elements at levels 15 and 90 in the inner plexiform layer. Furthermore, all types of AC doublets occur at levels of the inner plexiform layer where cholinergic and serotoninergic cell processes are absent. This finding indicates that the bulk of GABA+ synapses likely represent sites of GABAergic transmission. GABA+ AC → GABA− AC contacts are slightly more prevalent than GABA− AC → GABA+ AC contacts simply due to the predominance of GABA+ synapses, but are nevertheless common throughout the midst of the inner plexiform layer.

Innervation of Mb BC terminals

In view of the dominance of GABA+ synapses onto all BC types and the apparent GABAergic control of Mb BCs in particular, we reconstructed half of a type Mb BC in 42 vertical 90-nm-thick sections, starting from the center of the terminal, yielding a terminal width of 3.9 μm and a presumed total width of 7.8 μm, near the average for type Mb terminals. A representative tracing is illustrated in Figure 11 and points out key forms of connectivity. For example, process 43 is a typical reciprocal feedback contact that also engages in feedforward to profiles likely to be GCs that are postsynaptic to the same ribbon. However, process 43 and many other ACs also form synapses onto the BC at a distance from the ribbon, and these must also be viewed as reciprocal feedback synapses. This half-terminal contained 46 ribbons: 10 monads, 28 dyads, 7

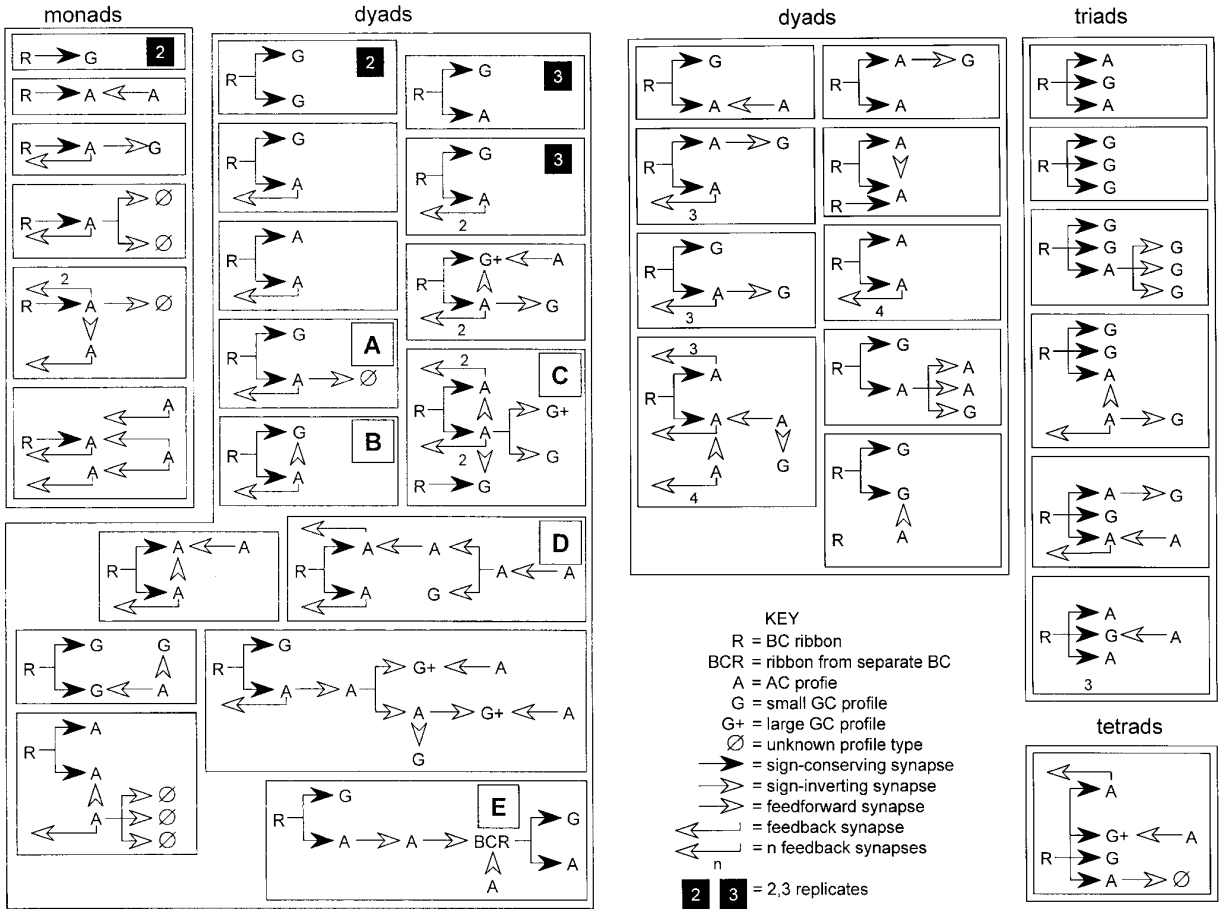

Fig. 12. Left and right: A comprehensive listing of all of the ribbon (R) and amacrine cell (AC) (A) conventional contacts made surrounding the Mb bipolar cell (BC) illustrated in Figure 8, including putative ganglion cell (GC) contacts. The data are separated into monads, dyads, triads, and tetrads representing ribbon sites where 1, 2, 3, and 4 profiles, respectively, demonstrated distinctive postsynaptic densities. Black block numbers indicate instances where 2 or 3 replicates of the connective pattern were documented. Small numbers above feedback arrows indicate numbers of separate synapses made by the same process. **A:** A generalized reciprocal feedback/feedforward pattern. **B:** A distinctive local reciprocal feedback/feedforward pattern for which the same AC targets both its input BC and the output GC from the same ribbon. **C:** A distinctive local complex, revealing both intensive reciprocal feedback, nested feedback and feedforward from a single ribbon input. **D:** A concatenated four-synapse AC chain targeting a BC terminal through a final AC element that also mediates reciprocal feedback. **E:** A two-synapse AC chain connecting the output of the Mb BC with a small neighboring small BC terminal (BCR).

triads, and 1 tetrad. Most of the monads were encountered in the sections beginning or ending the reconstruction, and, because we might have missed a small contact, likely better than 80% of all ribbons involve multiple contacts. Some contacts were unequivocally monads, usually onto AC profiles. There were 175 distinct AC synapses on the terminal and a single Mb BC terminal, thus, might be expected to have roughly 90 ribbons and 350 AC inputs. We identified 51 AC profiles adjacent to BC ribbons that displayed some form of contact: 14 were presynaptic only; 19 formed reciprocal feedback synapses; 11 formed both feedback and feedforward synapses; 7 formed feedforward synapses alone. Taken another way, 86% of these profiles had identified inputs to the BC, 59% were reciprocal, and 35% had nearby feedforward targets. Because it is quite clear that both feedforward and feedback targets can be far from the ribbon, these values must be lower limits and suggest that Mb terminals, at least, have a large number of contacts that engage in at least simple local feedback (see below).

The important issue at hand is the actual contact pattern exhibited by ACs. Figure 12 summarizes all the ribbon contacts made on this terminal and the associated AC contacts. Box A in Figure 12 demonstrates the generic dyad with both ganglion and ACs as targets and the AC forming a reciprocal feedback contact as well as a feedforward synapse onto an unidentified profile. Box B defines what may well be the standard AC contact: dual feedback/feedforward where feedback is sent "back" to the source stage (the BC) and feedforward is sent to the target (the GC). However, even those ACs engaging in reciprocal contacts participate in richer patterns of connectivity, as suggested by the high frequency of concatenated conventional synapses in the inner plexiform layer. First, an AC that

forms a reciprocal feedback synapse may also form feedforward contacts to a neighboring reciprocal AC (Fig. 12, box C): a pattern we term *nested feedback*. Second, paths as long as three AC synapses terminate on AC profiles that are part of the reciprocal feedback path of a BC (Fig. 12, box D). These are common forms of connectivity and this Mb BC reveals a large number of concatenations that may be partial views of the complex illustrated in box C: AC → AC → BC (9 cases); BC → AC → AC (8 cases); BC → AC ← AC (14 cases); BC ← AC → AC (four cases). In 51 AC contacts, we encounter 35 cases of local serial conventional synapses. Thus, two-thirds of the ACs engage in concatenated synapses and many of these are explicitly nested feedback synapses. As we could not reconstruct all the AC processes wrapping the BC and because many of them undoubtedly represent the same kind of AC, two-thirds must be a minimum fraction. Finally, clear instances of AC chains between different BCs emerge (Fig. 12, box E), where the second BC possessed a small terminal at the end of its axon and was clearly not of the Mb variety. Given that 92% of all AC profiles and 98% of those contacting BCs are GABA+, the paths seen here suggest concatenated inhibitions to be part of the basic circuitry of all BCs.

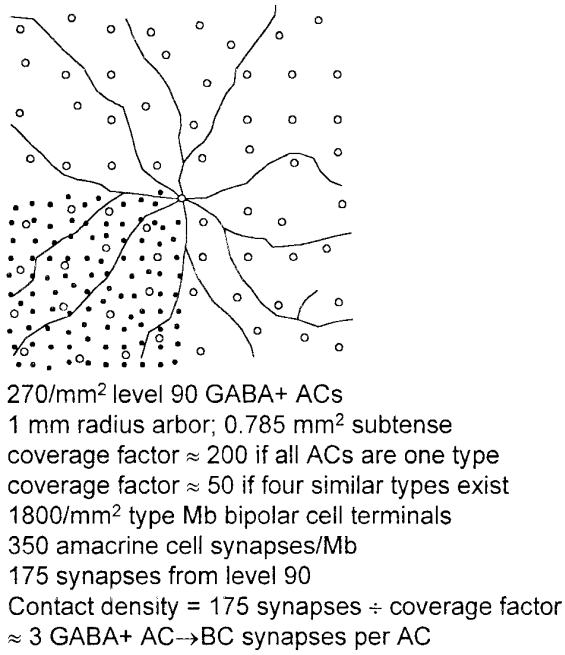

Fig. 13. The topology of pyriform γ-aminobutyrate-immunoreactive (GABA+) amacrine cells (ACs) that arborize at level 90 of the inner plexiform layer, mediating contacts with the proximal portion of Mb bipolar cells (BCs). Open circles represent idealized AC soma positions, and filled circles represent Mb BC terminal patterns. The line profile is taken from a Golgi-impregnated pyriform AC arborizing at level 90.

DISCUSSION

GABAergic connectivity in the inner plexiform layer revisited

GABA+ ACs dominate the circuitry of the inner plexiform layer and much of the organization of GC receptive fields must be influenced by GABA receptor biochemistry and biophysics. However, from the perspective of basic circuitry, simple feedforward or reciprocal feedback models fail to reflect the widespread occurrence of (1) nested feedback, (2) nested feedforward, (3) concatenated inhibitory, and (4) somatic inhibitory synapses. The first three may be the most common inhibitory micronetworks in the goldfish retina, yet few models of visual processing consider their properties. Serial conventional synapses and their possible physiologic roles have long been discussed. Similarly, synaptic configurations that we define as nested feedback were explicitly illustrated for amphibian and teleost retinas 3 decades ago (e.g., Fig. 15 in Dowling, 1968; Fig. 18 in Dowling and Werblin, 1969; and Fig. 17 in Witkovsky and Dowling, 1969). It is perhaps not too impetuous, then, to outline some limiting properties involving "serial" synapses and reconsider their possible functional attributes.

The identification of explicit reciprocal feedback synapses is often based on a fortuitous images near ribbons, but a single AC type can have looping or branching processes around a single BC terminal that form bona fide feedback synapses at a significant remove from any ribbon and still be "local" to the BC terminal (e.g., Fig. 11; also see the Discussion by Goldman and Fisher, 1978). If we consider the topologies associated with nested feedback, an individual AC likely makes few synapses per BC and targets other individual ACs *en passant* rather than its own dendrites. For example, goldfish Mb bipolar cells contact at least two groups of ACs (Marc et al., 1978; Yazulla et al., 1987) and AC contacts on the proximal half arise from monostratified pyriform ACs centered on level 90. There are probably four unique AC types in this group (types 1.7, 2.7, 3.7, and 12.7 of Wagner and Wagner, 1988), with an aggregate density of ≈270/mm^2 (Marc, 1982) and a typical maximal dendritic field diameter of ≈1 mm. Although Mb BCs represent three distinct cell types (Ishida et al., 1980), we presume that the overall AC synapse density is close to that reported here from reconstruction and as estimated by Witkovsky and Dowling (1969) from single section calculations: ≈300–350 AC synapses/terminal. If all proximal AC synapses arise from one cell type, the maximal density of synapses from a single AC upon one BC terminal would average ≈3 (Fig. 13); lumping AC groups only decreases the density. Thus, any nested synapses *around* the proximal half of given terminal would likely involve the same *type* of AC but not the same individual process. However, homologous coupling between sustained ON-center ACs in teleosts is well established (Teranishi et al., 1987; Hidaka et al., 1993; Teranishi and Negishi, 1994; Sakai et al., 1997), and all such AC dendrites in the vicinity of a given BC terminal might be considered an equivalent syncytium. The simplest type of nested feedback, thus, has an equivalent retinal topology shown in Figure 14A. If one argues that mixed types of noncoupled ACs are involved, the simplest topology is shown in Figure 14B, which collapses to the previous form upon coupling AC1 and AC2. Although it is still popular to consider the surrounds of BCs as largely derived from HCs, appropriate color-opponent surrounds could easily arise from ACs with direct inputs from red-dominated ON-center BCs driving ACs that selectively

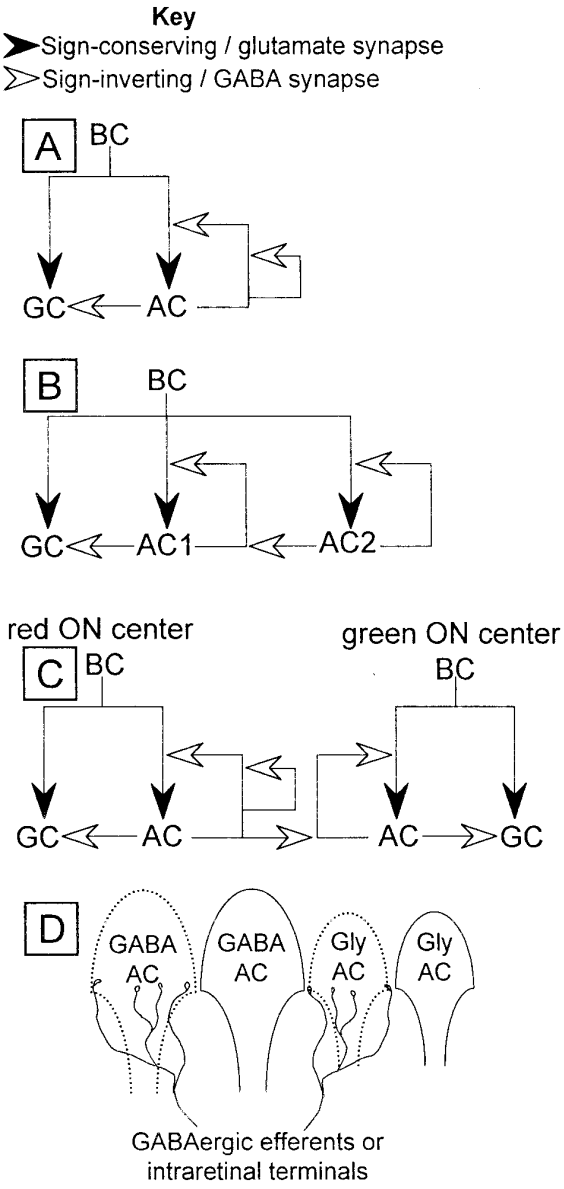

Fig. 14. The basic forms of γ-aminobutyrate (GABA)-ergic amacrine cell (AC) connectivity in the inner plexiform layer. **A:** The nested feedback synapse involving self-targeting, presuming that all AC contacts arise from the same type of AC. GC, ganglion cell. **B:** The nested feedback synapse involving two distinct types of ACs. **C:** A mixture of local nested feedback and concatenated feedforward demonstrating signal sharing between two different bipolar cell (BC) and AC sets. **D:** Conventional synapses onto GABAergic and glycinergic ACs arising from GABAergic efferents or intraretinal processes. Gly, glycine.

target green-dominated BCs, in lateral concatenated inhibitory feedback (Fig. 14C). Once we take the dendritic topologies of ACs into account, we encounter the possibility that simple feedback and feedforward may not exist at all; that they are simply the most probable configuration presented in thin section analyses.

Pure simple feedback and feedforward micronetworks may be associated with specific BC → GC complexes, but it is difficult to be guess what those might be. Even a simple circuit such as the primate midget BC → midget GC system (Kolb and Dekorver, 1991) clearly exhibits frequent AC → AC contacts that may be nested feedforward or feedback (Calkins and Sterling, 1996). The GABA+ A17-equivalent system targeting rod BCs in mammals appears to involve simple feedback at the BC terminal level (Strettoi et al., 1990), but need be viewed with caution as A17-equivalents receive significant AC input on their dendrites from different but likely GABAergic ACs (Nelson and Kolb, 1985; Sandell et al., 1989).

We invoke the unlovely adjective "concatenated" to emphasize the need for formal evaluation of the sign and gain of a synaptic chain. Anatomic serial synapses between presumed GABAergic ACs have been previously described by Vaughn et al. (1981), Zucker et al. (1984), Mariani and Caserta (1986); Muller and Marc (1990), Koontz et al. (1993) and because we now know that >90% of all conventional synapses in the teleost inner plexiform layer are GABA+, it is easy to conceive that most examples of serial conventional synapses are GABAergic. The interpretation that the majority of the synapses between GABA+ amacrine cells are GABAergic, rather than involving a colocalized neurotransmitter, is also based on the presumption that distinct conventional synaptic complexes associated with small electron lucent vesicles represent fast transmission elements. With the exception of dopaminergic interplexiform cells, all goldfish ACs are either GABA+, glycine+, or members of the dual GΓ1 class (Marc et al., 1995). In general, the synapses made by dopaminergic interplexiform cells are not as distinct as those described here, best characterized as "junctional complexes" rather than conventional synapses in two-thirds of their contacts (Yazulla and Zucker, 1988; but see Marshak, 1992), and they can represent at best only 0.5% of the profiles in the inner plexiform layer. S1 ACs (Marc et al., 1988b) are dual serotoninergic/GABAergic cells (Ball and Tutton, 1990) and bona fide serotoninergic synapses might indeed seem indistinguishable from GABA+ profiles. Even so, they can comprise only a small fraction of the AC profiles at levels 15 and 90 of the inner plexiform layer (Marc et al., 1988b) and most of the concatenated profiles in those zones must still be GABA+. Conversely, many of the AC synapses at levels 30 and 60 of the goldfish inner plexiform layer are formed by dual cholinergic/GABAergic ACs (Marc et al., 1993) that arborize in the zones of peak synapse frequency and GABA profile frequency distributions. Concatenated synapses in these zones could well involve cholinergic synaptic transfers, even cholinergic AC → cholinergic AC signaling, as the latter has been posited for starburst ACs (Millar and Morgan, 1987). Even so, GABAergic signaling clearly numerically dominates the cholinergic strata, even in mammals (Mariani and Hersh, 1988).

Although we do not know how to differentially recognize cholinergic and GABAergic synapses, this scenario prompts us to consider the consequences of concatenated excitations and inhibitions. Ionotropic receptors that gate cation fluxes with reversal potentials substantially more positive than the resting potential often display voltage gains greater than unity somewhere in their operating

ranges (Wu, 1988; Wu and Yang, 1992; Witkovsky et al., 1997; Yang and Wu, 1998). If this were true of ionotropic cholinergic synapses, extensive sign-conserving cholinergic starburst → starburst AC signaling might quickly ramp to a physiologic maximum, and a single photoresponse could propagate across the entire retina, not unlike the propagation of a photoreceptor signal through the glutamatergic afferent chain to the brain. However, starburst ACs have receptive fields only slightly larger than their dendritic arbors and show no evidence of intercellular signal propagation other than possible surround inhibition (Bloomfield, 1992; Taylor and Wässle, 1995). Muscarinic transmission between starburst ACs is possible, but at least some retinal muscarinic receptors fail to localize to starburst ACs (Wasselius et al., 1998). Thus, sign-conserving cholinergic → cholinergic transmission seems unlikely to exist in mammalian retinas (even at fractional synaptic gain), leaving the GABAergic starburst → starburst AC mode as the most plausible concatenation. Of course some of these synapses might be cholinergic → GABA AC synapses, but that pair can be formally collapsed to an equivalent sign-inverting step.

If we can extrapolate to teleosts, even within the "cholinergic" strata, signaling between ACs must most often involve chains of two or more sign-inversions. The concatenated inhibitory pair deserves some consideration, as it can be theoretically collapsed into a single net sign-conserving transfer. The key attribute of this form is that ionotropic inhibitory signaling most often involves activation of anion permeations not far from their reversal potentials, which typically engenders *fractional* synaptic gains much less than unity (Wu, 1991). This is also expressed as fractional feedback loop gains in inhibitory networks (e.g., Maltenfort et al., 1998). Such concatenated pairs will not propagate but rather attenuate signals at each transfer, while conserving polarity. A single sign-conserving synapse and a concatenated inhibitory pair are, thus, different devices; the latter possibly representing a stable biologic circuit element when sign-conserving polarity is required at low gain. Alternatively, one could take the view that it is the magnitude of the conductance increase at any one stage in this chain that truncates signal propagation by shunting. However, two inversions would effect a conductance *decrease* in a target and might actually enhance any other signal propagation. The actual behavior of elements in concatenated inhibitory chains is likely to be intermediate, that is, a mixture of effective inversions and shunting truncations, depending on how close a given element is to the reversal potential for the inhibitory conductance. That large conductance changes may occur close to the reversal potential forces synaptic gain to be low at inhibitory synapses. In any event, this makes chains of inhibitory elements unlikely to support significant signal spread. Because the vast majority of GABA− AC profiles in the inner plexiform layer are glycinergic, the various chains described in Figure 8 are likely glycinergic → GABAergic and GABAergic → glycinergic contacts. They also represent simple concatenated sign-inverting steps. Similar to the situation we propose for BC feedback, simple monosynaptic feedforward could well be an illusion, and merely a part of nested patterns in many instances (Fig. 14).

A brief evaluation of nested feedback

What could nested feedback or feedforward actually do in a circuit? Most of these synapses are likely inhibitory and, if one considers the basic anatomic version of nested feedback (Figs. 1C, 14B), the path from BC → AC → AC → BC forms an apparent positive feedback loop, which is potentially unstable when the output of the BC is used as a measure of circuit properties. It is not our intent to produce a formal model of nested feedback synapses, as others are more qualified for this task. We can demonstrate how nested feedback (Fig. 15A) might shape the outputs of BCs and, by extension, the inputs to GCs. We used network modeling software (Extend v 3.2.1) to simulate nested feedback, considering BC → target synapses as sign-conserving amplifier elements with gains of 2 and AC → target synapses as sign-inverting with gains of 0.75 and lower bandpass than the sign-conserving elements. These properties characterize stable networks, and the absolute parameter values are not critical for the demonstration. Nevertheless, nested feedback stability requires fractional sign-inverting feedback voltage gain. Simulated BC responses to impulse inputs in the absence of feedback were simple alpha-like responses. With simple feedback, the responses were faster, with significant undershoots before returning to baseline, characteristic of a mildly underdamped system. The primary effects of nested feedback were to diminish the undershoot, without attenuating the improved response speed, and to hold the output recovery phase closer to baseline, which might be critical for a target spiking cell, such as a ganglion cell (Fig. 15B). Stable nested feedback would seem to have interesting consequences for the frequency-response characteristics of BCs, more easily visualized by examining the power spectra of the network (Fig. 15C). Simple feedback enhances the peak frequency response by sacrificing the bandwidth of the system (because the frequency dependence of the feedback elements are assumed to be low pass), exemplified by the horizontal line denoting the range of gains within 3 db of the best gain. Nested feedback partially flattens the gain characteristic, apparently effecting a biologic version of operational amplifier compensation. Indeed, the current state-of-the-art in designing operational amplifiers involves *nested* transconductance-capacitance compensation (e.g., Xie et al., 1999). We suggest that, because the biologic circuitry is stable, the general properties of real nested feedback elements should not be very different from those demonstrated in this simple artificial model.

The attributes of GABA receptors will clearly influence the details of nested feedback circuits. In general, BCs express both $GABA_A$ and $GABA_C$ receptors (Feigenspan and Bormann, 1994a; Matthews et al., 1994; Lukasiewicz et al., 1994; Qian and Dowling, 1995; Koulen et al., 1997), whereas ACs and GCs seem dominated by $GABA_A$ receptors (Feigenspan and Bormann, 1994b; Greferath et al., 1994; Lukasiewicz and Werblin, 1994; Lukasiewicz and Shields, 1998). As $GABA_A$ receptors are thought to have lower GABA affinity and mediate more transient currents than $GABA_C$ receptors (e.g., Lukasiewicz and Shields, 1998), nested feedback might be activated far from threshold and be of only brief efficacy, further increasing its stability.

Feedforward synapses are chains in which the surround signaling features of ACs are passed directly to targets

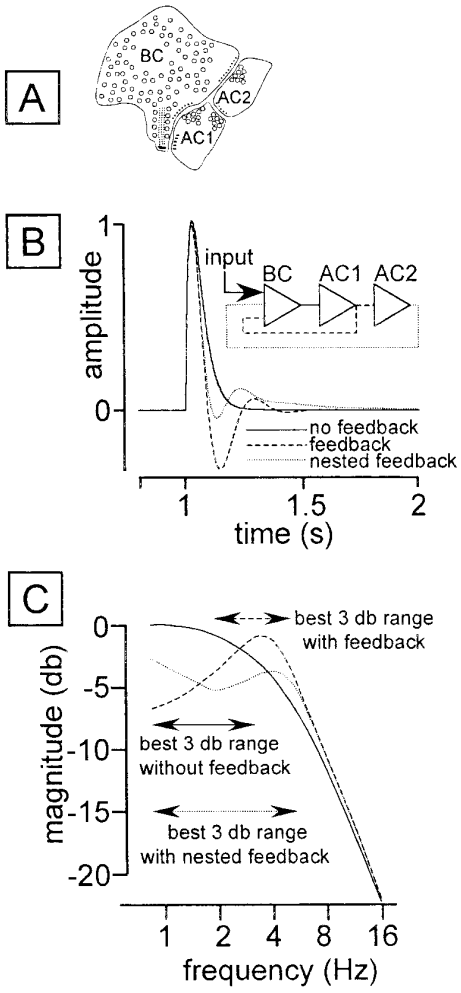

Fig. 15. Theoretical properties of nested feedback patterns. **A:** A typical nested feedback arrangement involving two separate amacrine cell (AC) processes. BC, bipolar cell. **B:** A series of modeled impulse responses by using a noninverting input to a model BC amplifier stage, a noninverting BC → AC1 input and sign-inverting inputs for all other paths. A simple monophasic response was generated through the model BC alone, followed by simple reciprocal feedback and nested feedback. **C:** Power spectra for the three configurations, displaying both the rolloff features and the best 3 db ranges (the frequency range where the gain remains within a factor of 2 of the peak gain) for each condition.

instead of being filtered once more through the BC synapse, although both configurations occur in parallel in some cases (Fig. 12). Although it is not our intent to compare the details of local feedback and feedforward (see Wu, 1992; Marc, 1992), the prevalence of two- and three-element inhibitory AC synaptic concatenations would seem to argue for their fundamental roles in receptive field organization. One might speculate that differential receptor thresholds, kinetics, and modulation states permit precise tuning of networks in ways that would be biologically cumbersome if circuitries were truly restricted to simple feedback and feedforward. Catfish ACs have been documented to engage in mutually sign-inverting connectivity by dual electrode experiments (Sakai and Naka, 1990), and, considering issues of encounter frequency, this finding suggests that such chaining of inhibition is the norm, not the exception.

Axosomatic synapses and efferents

Conventional synaptic drive of amacrine cells at the somatic level has been recognized for many years (Cowan and Powell, 1963; Dowling and Cowan, 1966), but other than for a few electrophysiologic studies (Miles, 1972; Marchiafava, 1976), recent efforts have emphasized modulatory peptidergic transmission (e.g., Stell et al., 1984). Our data suggest that many types of conventional GABAergic and glycinergic ACs receive direct GABAergic inputs at the somatic level (Fig. 14D), resembling circuitries of layer III and V pyramidal cells in primary visual cortex, which receive somatic synapses surrounding the primary axon by means of GABAergic basket cells (Freund et al., 1983). In those instances, strong local inhibition has the potential to globally attenuate spike generation. In the retina, AC somatic or dendritic spike generation could be attenuated or the synapses could simply hyperpolarize ACs and attenuate their synaptic outputs. Such a global GABAergic effect is consistent with Miles' (1972) observation that avian isthmo-optic tract myelinated efferents mediate surround disinhibition in the vast majority of cases. Alternatively, Marchiafava (1976) interpreted AC responses due to optic nerve stimulation as monosynaptic excitations in turtle and as evidence that all ACs receive a single efferent that saturates to yield an all-or-none response. Excitatory efferents might exist, but our data support neither evidence of conventional GABA− synapses onto ACs nor uniform efferent targeting of all cells. Rio et al. (1993) demonstrated GABA+ signals in 40% of the retinopetal efferent fibers encountered in lamprey, and these targeted both GABA+ and GABA− ACs. Although this is partially consistent with our findings, it raises both the question of the neurochemical identities of other efferents and the possibility of high false-negative rates in conventional electron microscopic immunocytochemical studies (see Appendix). Efferent fibers arise from several brain loci in fishes (Ebbeson and Meyer, 1981), but the coincident numbers of synapses and myelinated fibers at the distal margin of the inner plexiform layer (Fig. 9A, E) makes a strong case that most axosomatic synapses arise from the myelinated retinal efferents described by Witkovsky and Dowling (1969). In our hands, these were all GABA+. The profile of myelinated fibers through the inner plexiform layer suggests extensive axonal branching in the distal inner plexiform layer, that the branches themselves remain myelinated for some distance, and that the teleost retina should harbor a distinctive population of intraretinal oligodendrocytes. We were not able to encounter a transition between myelination and the final axon terminal expansion, but Witkovsky and Dowling (1969) clearly described extensive terminals that made many conventional synapses. We suggest that these are all fast inhibitory systems. Different efferent systems must exist, because the gonadotropin/FMRFamide-immunoreactive efferents of the cyprinid retina arising from *N. olfacotretinalis* are described as nonmyelinated (Ball et al., 1989), but also contain small, clear vesicles (Zucker and Dowling, 1987), suggesting that they too engage in fast neurotransmission.

SUMMARY

Our analysis of the goldfish inner plexiform layer clearly establishes the numerical dominance of GABAergic lateral transmission in the shaping of GC receptive fields. However, it is similarly clear that single-stage feedforward and reciprocal feedback might not be accurate descriptors of the vast majority of the inhibitory synaptic transfer paths between BCs and GCs. We suggest that nested feedback and feedforward are, in fact, the more likely topologies and hypothesize that such micronetworks might have superior performance attributes as feedback elements, analogous to compensation circuits in operational amplifiers. Chains of conventional synapses have been described since the inception of electron microscopic analysis of retina and have often been used as phylogenetic measures of retinal "complexity," but little else. We argue that this dominant mode of signaling is hardly one that can be eternally overlooked and that it is comprehensible. Most AC → AC transmission is sign-inverting but also likely possesses fractional gain, so concatenated inhibitions would not likely propagate far. Serial pairs, thus, can be collapsed into formal sign-conserving stages with unique low gain, focal attributes quite distinct from conventional ribbon-based, high gain, propagating sign-conserving synapse chains. The thresholds, kinetics, and modulation properties of GABA receptors will influence these features and offer more ways to tune receptive fields than simple feedforward and feedback. Finally, several GABA+ and GABA− AC types are targeted by GABA+ synapses at the somatic level and most of these arise from myelinated efferents. Although it is necessary to continue modeling retinal circuitry in isolation, it is clear that many ectotherms use multiple central systems to modify the efficacies of AC transmission through fast neurotransmitters such as GABA.

LITERATURE CITED

Ammermüller J, Weiler R. 1981. The ramification pattern of amacrine cells within the inner plexiform layer of the carp retina. Cell Tiss Res 220:699–723.

Ball AK, Tutton DA. 1990. Contacts between S1 amacrine cells and "I1" interplexiform cells in the goldfish retina. Invest Ophthalmol Vis Sci Suppl 33:1405.

Ball AK, Stell WK, Tutton DA. 1989. Efferent projections to the goldfish retina. In: Weiler R, Osborne NN, editors. Neurobiology of the inner retina. NATO ASI series, vol. H31. Berlin: Springer-Verlag. p 103–116.

Bloomfield S. 1992. Relationship between receptive and dendritic field size of amacrine cells in the rabbit retina. J Neurophysiol 68:711–725.

Calkins DJ, Sterling P. 1996. Absence of spectrally specific lateral inputs to midget ganglion cells in primate retina. Nature 381:613–615.

Cowan WM, Powell TPS. 1963. Centrifugal fibres in the avian visual system. Proc R Soc Lond B 158:232–252.

Dowling JE. 1968. Synaptic organization of the frog retina: an electron microscopic analysis comparing the retinas of frogs and primates. Proc R Soc Lond B 170:205–228.

Dowling JE, Cowan WM. 1966. An electron microscopic study of normal and degenerating centrifugal fiber terminals in the pigeon retina. Z Zellforsch 71:14–28.

Dowling JE, Werblin F. 1969. Organization of the retina of the mudpuppy, *Necturus maculosus*. I. Synaptic structure. J Neurophysiol 32:315–388.

Ebbeson SOE, Meyer DL. 1981. Efferents to the retina have multiple sources in teleost fish. Science 214:924–926.

Euler T, Wässle H. 1998. Different contributions of $GABA_A$ and $GABA_C$ receptors to rod and cone bipolar cells in a rat retinal slice preparation. J Neurophysiol 79:1384–1395.

Feigenspan A, Bormann J. 1994a. Differential pharmacology of $GABA_A$ and $GABA_C$ receptors on rat retinal bipolar cells. Eur J Pharmacol Mol Pharmacol 18:97–104.

Feigenspan A, Bormann J. 1994b. Facilitation of GABAergic signaling in the retina by receptors stimulating adenylate cyclase. Proc Natl Acad Sci USA 91:10893–10897.

Freed MA. 1992. GABAergic circuits in the mammalian retina. In: Mize R, Marc RE, Sillito A, editors. GABA in the retina and central visual system. Amsterdam: Elsevier. p 107–131.

Freed MA, Nakamura Y, Sterling P. 1983. Four types of amacrines in the cat retina that accumulate GABA. J Comp Neurol 219:295–304.

Freund TF, Martin KAC, Smith AD, Somogyi P. 1983. Glutamate decarboxylase-immunoreactive terminals of Golgi-impregnated axoaxonic cells and of presumed basket cells in synaptic contact with pyramidal cells of the cat's visual cortex. J Comp Neurol 221:263–278.

Goldman KA, Fisher SK. 1978. Synaptic organization of the inner plexiform layer of the retina of *Xenopus laevis*. Proc R Soc Lond B 201:57–72.

Greferath U, Gruenter U, Müller F, Wässle H. 1994. Localization of $GABA_A$ receptors in the rabbit retina. Cell Tissue Res 276:295–307.

Hidaka S, Maehara M, Umino O, Lu Y, Hashimoto Y. 1993. Lateral gap junction connections between retinal amacrine cells summating sustained responses. Neuroreport 5:29–32.

Hitchcock PF, Easter SE Jr. 1986. Retinal ganglion cells in goldfish: a qualitative classification into four morphological types and a quantitative study of the development of one of them. J Neurosci 6:1037–1050.

Ishida AT, Stell WK, Lightfoot DO. 1980. Rod and cone inputs to bipolar cells in goldfish retina. J Comp Neurol 191:315–335.

Kalloniatis M, Tomisch G. 1999. Amino acid neurochemistry of the vertebrate retina. Prog Retinal Eye Res 18:811–866.

Kalloniatis M, Marc RE, Murry RF. 1996. Amino signatures in the primate retina. J Neurosci 16:6807–6829.

Kelly JS, Weitch-Dick F. 1978. Critical evaluation of the use of radioautography as a tool in the localization of amino acids in the mammalian nervous system. In: Fonnum F, editor. Amino acids as chemical transmitters. New York: Plenum. p 102–121.

Kolb H, Dekorver L. 1991. Midget ganglion cells of the parafovea of the human retina: a study by electron microscopy and serial section reconstructions. J Comp Neurol 303:617–636.

Koontz MA, Hendrickson LE, Brace ST, Hendrickson AE. 1993. Immunocytochemical localization of GABA and glycine in amacrine and displaced amacrine cells of macaque monkey retina. Vision Res 18:2617–2628.

Kondo H, Toyoda J-I. 1983. GABA and glycine effects on the bipolar cells of the carp retina. Vision Res 23:1259–1264.

Koulen P, Brandstätter JH, Kroeger S, Enz R, Bormann J, Wässle H. 1997. Immunocytochemical localization of the $GABA_C$ receptor rho subunits in the cat, goldfish, and chicken retina. J Comp Neurol 380:520–532.

Lukasiewicz PD, Shields CR. 1998. Different combination of $GABA_A$ and $GABA_C$ receptors confer distinct temporal properties to retinal synaptic responses. J Neurophysiol 79:3157–3167.

Lukasiewicz PD, Werblin FS. 1994. A novel GABA receptor modulates synaptic transmission from bipolar to ganglion and amacrine cells in the tiger salamander retina. J Neurosci 14:1213–1223.

Lukasiewicz PD, Maple BR, Werblin FS. 1994. A novel GABA receptor on bipolar cell terminals in the tiger salamander retina. J Neurosci 14: 1202–1212.

Maltenfort MG, Heckman CJ, Rymer WZ. 1998. Decorrelating actions of Renshaw interneurons on the firing of spinal motoneurons within a motor nucleus: a simulation study. J Neurophysiol 80:309–323.

Marc RE. 1982. Spatial organization of neurochemically classified interneurons in the goldfish retina: I. Local patterns. Vision Res 22:589–608.

Marc RE. 1986. Neurochemical stratification in the inner plexiform layer of the vertebrate retina. Vision Res 26:223–238.

Marc RE. 1989. The anatomy of multiple GABAergic and glycinergic pathways in the inner plexiform layer of the goldfish retina. In: Weiler R, Osborne NN, editors. Neurobiology of the inner retina, NATO ASI Series, Vol. H31a. Berlin: Springer-Verlag. p 53–64.

Marc RE. 1992. The structure of GABAergic circuits in ectotherm retinas. In: Mize R, Marc RE, Sillito A, editors. GABA in the retina and central visual system. Amsterdam: Elsevier. p 61–92.

Marc RE, Lam DMK. 1981. Glycinergic pathways in the goldfish retina. J Neurosci 1:152–165.

Marc RE, Liu W-LS. 1985. Glycine-accumulating neurons in the human retina. J Comp Neurol 232:241–260.

Marc RE, Stell WK, Bok D, Lam DMK. 1978. GABAergic pathways in the goldfish retina. J Comp Neurol 182:221–246.

Marc RE, Liu W-LS , Muller JF. 1988a. Gap junctions in the inner plexiform layer of the goldfish retina. Vision Res 28:9–24.

Marc, RE, Liu W-LS, Scholz K, Muller JF. 1988b. Serotonergic pathways in the goldfish retina. J Neurosci 8:3427–3450.

Marc RE, Liu W-LS, Kalloniatis M, Raiguel S, Van Haesendonck S. 1990. Patterns of glutamate immunoreactivity in the goldfish retina. J Neurosci 10:4006–4034.

Marc RE, Li H-B, Kalloniatis M, Arnold J. 1993. Cholinergic subsets of GABAergic amacrine cells in the goldfish retina. Invest Ophthalmol Vis Sci Suppl 34:1061.

Marc RE, Basinger SF, Murry RF. 1995. Pattern recognition of amino acid signatures in retinal neurons. J Neurosci 15:5106–5129.

Marchiafava PL. 1976. Centrifugal actions on amacrine and ganglion cells in the retina of the turtle. J Physiol 255:137–155.

Mariani AP, Caserta MT. 1986. Electron microscopy of glutamate decarboxylase (GAD) immunoreactivity in the inner plexiform layer of the rhesus monkey retina. J Neurocytol 15:645–655.

Mariani AN, Hersh LB. 1988. Synaptic organization of cholinergic amacrine cells in the rhesus monkey retina. J Comp Neurol 267:269–280.

Marmarelis PZ, Marmarelis VZ. 1978. Analysis of physiological systems. New York: Plenum Press. 487 p.

Marshak D. 1992. Localization of immunoreactive tyrosine hydroxylase in the goldfish retina with pre-embedding immunolabeling with one-nanometer colloidal gold particles and gold toning. J Histochem Cytochem 40:1465–1470.

Marshak D, Ariel M, Brown E. 1988. Distribution of synaptic inputs onto goldfish retinal ganglion cell dendrites. Exp Eye Res 46:965–978.

Massey SC. 1990. Cell types using glutamate as a neurotransmitter in the vertebrate retina. Prog Retinal Res 9:399–425.

Matthews G, Ayoub GS, Heidelberger R. 1994. Presynaptic inhibition by GABA is mediated via two distinct GABA receptors with novel pharmacology. J Neurosci 14:1079–1080.

Miles FA. 1972. Centrifugal control of the avian retina: III. Effects of electrical stimulation of the isthmo-optic tract on the receptive field properties of retinal ganglion cells. Brain Res 48:115–129.

Millar TJ, Morgan IG. 1987. Cholinergic amacrine cells in the rabbit retina synapse onto other cholinergic amacrine cells. Neurosci Lett 74:281–285.

Muller JF, Marc RE. 1990. GABA-ergic and glycinergic pathways in the inner plexiform layer of the goldfish retina. J Comp Neurol 291:281–304.

Muller JF, Ammermüller J, Normann RA, Kolb H. 1991. Synaptic inputs to physiologically defined turtle retinal ganglion cells. Vis Neurosci 7:409–429.

Nakamura Y, McGuire BA, Sterling P. 1980. Interplexiform cell in cat retina: identification by uptake of gamma-(^{3}H)-aminobutyric acid serial reconstruction. Proc Natl Acad Sci USA 77:658–661.

Nelson R, Kolb H. 1985. A17: a broad-field amacrine cell in the rod system of the cat retina. J Neurophysiol 54:592–614.

Ottersen OP, Madsen S, Storm-Mathisen J, Somogyi P, Scopsi L, Larsson L-I. 1988. Immunocytochemical evidence suggests that taurine is colocalized with GABA in Purkinje cell terminals, but that the stellate cell terminals predominantly contain GABA: a light- and electronmicroscopic study of the rat cerebellum. Exp Brain Res 72:407–416.

Pourcho RG. 1981. Autoradiographic Localization of [^{3}H]muscimol in the cat retina. Brain Res 215:187–199.

Pourcho RG, Goebel DJ. 1983. Neuronal subpopulations in cat retina which accumulate the GABA agonist, (^{3}H)muscimol: a combined Golgi and autoradiographic study. J Comp Neurol 219:25–35.

Qian H, Dowling JE. 1995. $GABA_A$ and $GABA_C$ receptors on hybrid bass retinal bipolar cells. J Neurophysiol 74:1920–1928.

Ramón y Cajal S. 1892. La retinédes vertébrés. La Cellule, vol 9.

Rio JP, Vesselkin NP, Kirpitchnikova E, Kenigfest NB, Versaux-Botteri C, Reperant J. 1993. Presumptive GABAergic centrifugal input to the lamprey retina: a double-labeling study with axonal tracing and GABA immunocytochemistry. Brain Res 600:9–19.

Sakai HM, Naka K-I. 1990. Dissection of the neuron network in the catfish inner retina V. Interactions between NA and NB amacrine cells. J Neurophysiol 63:120–130.

Sakai HM, Machuca H, Naka K-I. 1997. Processing of color- and noncolor-coded signals in the gourami retina: II. Amacrine cells. J Neurophysiol 78:2018–2033.

Sandell JH, Masland RH, Raviola E, Dacheux RF. 1989. Connections of indoleamine-accumulating cells in the rabbit retina. J Comp Neurol 283:303–313.

Scholes JH. 1975. Colour receptors and their synaptic connexions in the retina of a cyprinid fish. Philos Trans R Soc Lond B 270:61–118.

Sherry DM, Yazulla S. 1993. Goldfish bipolar cells and axon terminal patterns: a Golgi study. J Comp Neurol 329:188–200.

Somogyi P, Halasy K, Somogyi J, Storm-Mathisen J, Ottersen OP. 1986. Quantification of immunogold labelling reveals enrichment of glutamate in mossy and parallel fibre terminals in cat cerebellum. Neuroscience 19:1045–1050.

Stell WK, Walker SE, Chohan KS, Ball AK. 1984. The goldfish nervus terminalis: a luteinizing hormone-releasing hormone and molluscan cardioexcitatory peptide immunoreactive olfactoretinal pathway. Proc Natl Acad Sci USA 81:940–944.

Stell WK, Walker SE, Ball AK. 1987. Functional anatomical studies on the terminal nerve projection to the retina of bony fishes. Ann N Y Acad Sci 519:80–96.

Storm-Mathisen J, Leknes AK, Bore AT, Vaaland JL, Edminson P, Huang FMS, Ottersen OP. 1983. First visualization of glutamate and GABA in neurons by immunocytochemistry. Nature 301:517–520.

Strettoi E, Dacheux RF, Raviola E. 1990. Synaptic connections of rod bipolar cells in the inner plexiform layer of the rabbit retina. J Comp Neurol 295:449–466.

Studholme KM, Yazulla S. 1988. Localization of GABA and glycine in goldfish retina by electron microscopic postembedding immunocytochemistry: improved visualization of synaptic structures with LR white resin. J Neurocytol 17:859–870.

Swain PH, Davis SM. 1978. Remote sensing: a quantitative approach. New York: McGraw-Hill.

Tachibana M, Kaneko A. 1987. γ-Aminobutyric acid exerts a local inhibitory action on the axon terminal of bipolar cells: evidence for negative feedback from amacrine cells. Proc Natl Acad Sci USA 84:3501–3505.

Taylor WR, Wässle H. 1995. Receptive field properties of starburst cholinergic amacrine cells in the rabbit retina. Eur J Neurosci 7:2308–2321.

Teranishi T, Negishi K. 1994. Double-staining of horizontal and amacrine cells by intracellular injection with Lucifer Yellow and biocytin in carp retina. Neuroscience 59:217–226.

Teranishi T, Negishi K, Kato S. 1987. Functional and morphological correlates of amacrine cells in carp retina. Neuroscience 20:935–950.

Thoreson WB, Witkovsky P. 1999. Glutamate receptors and circuits in the vertebrate retina. Prog Retinal Eye Res 18:765–810.

Todd AJ, Watt C, Spike RC, Sieghart W. 1996. Colocalization of GABA, glycine, and their receptors at synapses in the rat spinal cord. J Neurosci 16:974–982.

Uchiyama H, Reh T, Stell WK. 1988. Immunocytochemical and morphological evidence for a retinopetal projection in anuran amphibians. J Comp Neurol 274:48–59.

Vaughn JE, Famiglietti EV Jr, Barber RP, Saito K, Roberts E, Ribak CE. 1981. GABAergic amacrine cells in rat retina: immunocytochemical identification and connectivity. J Comp Neurol 197:113–127.

Wagner H-J, Wagner E. 1988. Amacrine cells in the retina of a teleost fish the roach (*Rutilus rutilus*): a Golgi study on differentiation and layering. Philos Trans R Soc Lond B 321:263–324.

Wasselius J, Johansson K, Bruun A, Zucker C, Ehinger B. 1998. Correlations between cholinergic neurons and muscarinic m2 receptors in the rat retina. Neuroreport 9:1799–1802.

Witkovsky P. 1971. Synapses made by myelinated fibers running to teleost and elasmobranch retinas. J Comp Neurol 142:205–222.

Witkovsky P, Dowling JE. 1969. Synaptic relationships in the plexiform layers of the carp retina. Z Zellforsch 100:60–82.

Witkovsky P, Stell WK. 1973. Retinal structure in the smooth dogfish *Mustelis canis:* electron microscopy of serially sectioned bipolar cell synaptic terminals. J Comp Neurol 150:147–168.

Witkovsky P, Schmitz Y, Akopian A, Krizaj D, Tranchina D. 1997. Gain of rod to horizontal cell synaptic transfer: relation to glutamate release and a dihydropyridine-sensitive calcium current. J Neurosci 17:7297–7306.

Wu SM. 1988. Synaptic transmission from rods to horizontal cells in dark-adapted tiger salamander retina. Vision Res 28:1–8.

Wu SM. 1991. Input-output relations of the feedback synapse between

horizontal cells and cones in the tiger salamander retina. J Neurophysiol 28:1–8.

Wu SM. 1992. Functional organization of GABAergic circuits in ectotherm retinas. In: Mize R, Marc RE, Sillito A, editors. GABA in the retina and central visual system. Amsterdam: Elsevier. p 93–106.

Wu SM, Yang X-L. 1992. Modulation of synaptic gain by light. Proc Natl Acad Sci USA 89:11755–11758.

Wülle I, Wagner HJ. 1990. GABA and tyrosine hydroxylase immunocytochemistry reveal different patterns of colocalization in retinal neurons of various vertebrates. J Comp Neurol 296:173–178.

Xie X, Schnieder MC, Sánchez-Sinencio E, Embabi SHK 1999. Sound design of low power nested transconductance-capacitance compensation amplifiers. IEEE Electronics Letters 35:956–958.

Yang XL, Wu SM. 1997. Response sensitivity and voltage gain of the rod- and cone-bipolar cell synapses in dark-adapted tiger salamander retina. J Neurophysiol 78:2662–2673.

Yazulla S. 1981. GABAergic synapses in the goldfish retina: An autoradiographic study of ^{3}H-muscimol and ^{3}H-GABA binding. J Comp Neurol 200:83–93.

Yazulla S, Zucker CL. 1988. Synaptic organization of dopaminergic interplexiform cells in the goldfish retina. Vis Neurosci 1:13–29.

Yazulla S, Studholme KM, Wu J-Y. 1987. GABAergic input to the synaptic terminals of mb_1 bipolar cells in the goldfish retina. Brain Res 411: 400–405.

Zucker CL, Dowling JE. 1987. Centrifugal fibres synapse on dopaminergic interplexiform cells in the teleost retina. Nature 330:166–168.

Zucker CL, Yazulla S, Wu J-Y. 1984. Non-correspondence of [^{3}H] GABA uptake and GAD localization in goldfish amacrine cells. Brain Res 298:154–158.

APPENDIX

Classification error

Estimating assignment errors in a spatial system requires full histograms of signals sampled from "model" elements known to be GABA+ and GABA−. Such data are difficult to acquire with either autoradiography or electron microscopic (EM) immunogold immunocytochemistry, and it is standard practice to use granule label density over samples of accepted signal positive and negative tissue regions to estimate mean signal-to-noise ratios (SNRs). This method usually provides an upper bound for the error rate.

SNR values for EM autoradiography for transported ligands such as [^{3}H]GABA and [^{3}H]glycine, have been reported to be as high as 32:1 (Muller and Marc, 1990) but are usually lower. We calculated the apparent SNR for autoradiographic data in Marc and Liu (1985) to average 10:1 with a low of 5:1 in neuropil and a high of 17:1 for somas. Thus, in neuropil, the probability of making a false assignment can range up to 20%. Moreover, mean grain densities lower than 4 grains per structure (unit counting area) designed to lower backgrounds or shorten exposures also radically increase the rate of false negatives: the rate of zero grain occurrences in truly labeled elements (Kelly and Weitch-Dick, 1978). By using average grain densities as low as 3 in labeled profiles (a rather common practice for small structures like synapses) one can calculate directly from the Poisson equation that 5% of truly labeled elements will have no grains. If the *label criterion* is also set at 3, 46% or nearly half of truly labeled elements will be classified incorrectly as unlabeled. Only with very high synaptic label rates and robust criteria (10 grain mean, 5 grain criterion) does the theoretical false-negative rate drop below 5% at the cost of increasing false-positive rates due to grain spread (see below). Apparent SNR values are aggregate figures of merit determined not only by the physics of signal formation and sample area but also the biology of signal incorporation. These factors, among others, have made EM autoradiography justly unpopular for population analyses.

Because EM immunogold methods have intrinsically higher resolution than autoradiography, their potential applicability for quantitative work is higher. However, for various reasons beyond the scope of this manuscript, EM immunogold methods for detecting endogenous GABA or glycine immunoreactivities typically have *lower* SNR values than EM autoradiography of high-affinity uptake. SNR values for EM immunogold GABA immunoreactivities calculated from published images were remarkably similar across laboratories and tissues: 6.5 ± 1.7 for cerebellum (Ottersen et al., 1988; Somogyi et al., 1986), 8.6 ± 1.6 for spinal cord (Todd et al., 1996), and 6.6 ± 2.7 for retina (Studholme and Yazulla, 1988). Muller et al. (1991) reported SNR values for amino acid immunocytochemistry by EM immunogold visualization in turtle retina over a 5:1–9:1 range. Our own best results with EM immunogold rarely exceeded 10:1. In general, it is safe to say that ultrastructural assignments in neuropil by using immunogold methods for GABA immunoreactivity achieve approximately a 10% error rate provided an adequate granule density is used. However, publications clearly using lower granule means and criteria are legion. We will not discuss enzyme-linked methods beyond noting that it is virtually impossible to define SNR values in most cases and that the method is highly predisposed to false-negative errors due to the nonlinearity of the enzyme amplification procedure.

Direct comparisons of error rates with overlay microscopy are difficult because the sampling method is different and pixel value scaling does not correlate directly with granule number. However, because silver intensification is a continuous tone image, the probability of error for overlay microscopy is the sum of the false-positive and false-negative rates which are, in turn, the integrated GABA+/GABA− and GABA−/GABA+ ratios above and below a given decision boundary, respectively (Swain and Davis, 1978; Marc et al., 1995). Appendix Figure 1A shows typical Gaussian envelope fits to histogrammed data derived from GABA+ and GABA− inner plexiform layer regions in specimen S371 used in this study. The probability of error $<<0.001$ for any kind of classification by using overlay microscopy with our signal visualization tactics. Unlike autoradiography or EM immunogold visualization, detection of signals by silver-intensified LM methods is effectively errorless.

Spatial resolution

The operational resolutions of these three methods vary considerably. Theoretical resolutions of autoradiography and EM immunogold methods are rarely achieved because biologic and mathematical constraints force the selection of mean and criterion label densities. These criteria are typically defined post hoc in a subjective attempt to limit false-*positive* assignments and always incur the SNR problems and false-negative rates noted above. This impacts the practical resolution of a method in defining the minimum area encompassed by a criterion cluster of grains at a given mean density. Thus, we compared practical spatial resolutions of the aforementioned methods by determining the diameters of areas encompassed by criterion groupings of silver grains or gold granules in published EM images.

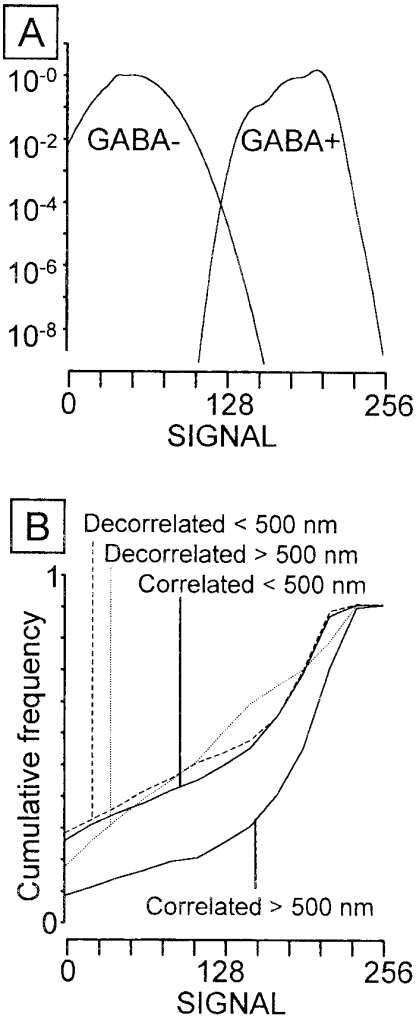

Fig. A1. Parametric features of overlay microscopy relevant for ultrastructural mapping of synaptic populations. **A:** Pixel intensity probability histograms for optical microscopy of GABA immunoreactivity on ultrathin sections for all presumed GABA+ profiles versus all other pixels in the image. The histograms were modeled as sums of Gaussians, normalized to 1, and plotted on logarithmic probability ordinates. The crossover point indicates a signal-to-noise ratio of $\approx 10^{-4}$. **B:** Cumulative frequency histograms reflecting quality-of-alignment properties for optical microscopy. Images of profiles smaller than 500 nm in diameter do not produce patterns of alignments significantly different from decorrelated (random) alignments of any size, whereas profiles larger than 500 produce alignments significantly precise to permit unambiguous differentiation from a random pattern with $P \leq 0.01$ (Kolmogorov-Smirnov test).

By using our own amino acid transport data with autoradiographic grains visualized by physical development (Marc and Liu, 1985; Muller and Marc, 1990), we estimated the practical minimal resolution as the diameter of a circle encompassing a criterion group of 4 grains: 642 ± 146 nm (n = 37 samples). In practice, profiles smaller than 600 nm in diameter have increasing risk of erroneous classification. EM immunogold preparations have the best resolution of all the methods tested. By using the same references for which SNR values were estimated, we calculated a criterion 4 granule resolution of 194 ± 53 nm (n = 18 samples). A resolution of 200 nm seems standard for EM immunogold visualization with the proviso that an acceptable SNR exists. However, close examination of many published EM immunogold images reveals deviations from these salutary examples, with both poor spatial resolution and poor SNR. Enzyme-linked methods provide exceptional spatial localization.

As overlay images are continuous tone, resolution was estimated by examples of individual resolution events (Figs. 3–8) and formally assessed by statistical analysis of the quality of alignment of GABA+ LM profiles onto EM profiles. Alignment analysis compared histograms of signal strength in electron microscopically identified structures for correlated (registered) versus decorrelated images and was executed in the ImagePro® Plus image processing environment (Media Cybernetics, Silver Spring, MD). Correlated data sets were generated by using an EM image registered to a binary mask of various disk sizes that represented the full spectrum of profile sizes in the image. Each EM profile was covered by the largest disk of pixel value 0 (PV = 0, black) that could fit within its borders. After all the usable profiles were filled, the entire nondisk background was assigned PV 255 (white). This method generated a mask of black disks whose diameter distribution reflected the mean circular diameters of the underlying profiles and ranged from 100–1,000 nm. This mask was subtracted from the binarized version of a correlated GABA+ LM image. The final data set, thus, was composed of virtual circles representing electron microscopic profiles containing various amounts of white signal, reflecting the degree of alignment of GABA+ and GABA− regions with particular sizes of profiles. As a corollary, the same mask of disks was subtracted from a noncorresponding image from S371 to produce a decorrelated or noise data set. The data were expressed as one frequency histogram of signal strengths for each range of profile diameters. Signal strength for each profile size range was the ratio of the sum of all individual PVs to the pixel area of a profile. Thus, a fully filled disk is intensity 255 (i.e., all pixels in the profile were GABA+), half filled is 128, and empty is 0 (all pixels in the profile were GABA−). A good alignment produces many disks with values near 255, whereas poor or random alignment yields a spectrum of gray values. These data were assembled as cumulative frequency histograms for different size groupings (Appendix Fig. 1B), and differences among them were evaluated with the Kolmogorov-Smirnov goodness of fit test. The null hypothesis was that the spectrum of signal strengths in profiles aligned randomly was indistinguishable from a registered set. The alternative hypothesis was that, at some size scale, the frequency distribution of signals in correlated images would converge on a pattern of unfilled and filled values, whereas the signals in the uncorrelated images would be smeared across a range of partially filled profiles. Thus, we sought the size distribution at which the Kolmogorov-Smirnov test yielded a highly significant difference between correlated and decorrelated images. Appendix Figure 1B summarizes the data for 1,096 profiles and demonstrates that the cutoff is 500 nm for overlay microscopy. For all profiles 500 nm or larger, overlay microscopy yields a statistically unique association of signal strengths

with profiles, rejecting the null hypothesis at better than P = 0.01. Thus, overlay microscopy yields robust spatial data down to 500 nm *in the absence of any other information*. However, unambiguous assignments can be achieved for many profiles even in the presence of substantial misalignment (e.g., profile displacement in serial sections), because the confluent overlay signal defines the shape of the labeled entity which the user can readily associate with an ultrastructural profile. The Rayliegh limit for optical microscopy is around 250 nm, but this method assumes no external information, such as the shapes and locations of possible sources. Most of the synaptic terminals presented in this manuscript were, in fact, larger than 500 nm along some axis. In general, the practical resolution of overlay microscopy should be expected to be 500 nm in *unfavorable* conditions (a field of similarly sized, closely spaced profiles) and perhaps as good as EM immunogold (approximately 250 nm) when local shape information is particularly good.

Summary

Overlay microscopy has substantial advantages over other amino acid visualization techniques. It is fast, archival, compatible with quantitative analyses, requires no manipulation of the electron microscopic specimen and preserves optimal ultrastructural visualization while providing nearly errorless signal identification with appropriate probes. The clear disadvantages are (1) the requirements for digital imaging resources and registration tools and the (2) the inferior resolution to good EM immunogold protocols. The latter feature is not a serious impediment in the global identification of synaptic profiles, because such structures are usually larger than 500 nm. When tracing small processes through serial sections, direct immunogold procedures will yield more satisfactory results.

APPENDIX LITERATURE CITED

Kelly JS, Weitch-Dick F. 1978. Critical evaluation of the use of radioautography as a tool in the localization of amino acids in the mammalian nervous system. In: Fonnum F, editor. Amino Acids as Chemical Transmitters. New York: Plenum. p 102–121.

Marc RE, Liu W-LS. 1985. Glycine-accumulating neurons in the human retina. J Comp Neurol 232:241-260.

Muller JF, Ammermüller J, Normann RA, Kolb H. 1991. Synaptic inputs to physiologically defined turtle retinal ganglion cells. Visual Neurosci 7:409–429.

Ottersen OP, Madsen S, Storm-Mathisen J, Somogyi P, Scopsi L, Larsson L-I. 1988. Immunocytochemical evidence suggests that taurine is colocalized with GABA in Purkinje cell terminals, but that the stellate cell terminals predominatly contain GABA: a llight- and electronmicroscopic study of the rat cerebellum. Exp Brain Res 72:407–416.

Somogyi P, Halasy K, Somogyi J, Storm-Mathisen J, Ottersen OP. 1986. Quantification of immunoglod lebelling reveals enrichment of glutamate in mossy and parallel fibre terminals in cat cerebellum. Neuroscience 19:1045–1050.

Todd AJ, Watt C, Spike RC, Sieghart W. 1996. Colocalization of GABA, glycine, and their receptors at synapses in the rat spinal cord. J Neurosci 16:974–982.